

AD/

Quarterly Technical Report

Solid State Research

1985:1

Lincoln Laboratory

MASSACHUSETTS INSTITUTE OF TECHNOLOGY

LEXINGTON, MASSACHUSETTS



Prepared under Electronic Systems Division Contract F19628-85-C-0002.

Approved for public release; distribution unlimited.

ADA160922

The work reported in this document was performed at Lincoln Laboratory, a center for research operated by Massachusetts Institute of Technology, with the support of the Department of the Air Force under Contract F19628-85-C-0002.

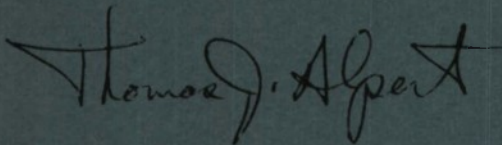
This report may be reproduced to satisfy needs of U.S. Government agencies.

The views and conclusions contained in this document are those of the contractor and should not be interpreted as necessarily representing the official policies, either expressed or implied, of the United States Government.

The ESD Public Affairs Office has reviewed this report, and it is releasable to the National Technical Information Service, where it will be available to the general public, including foreign nationals.

This technical report has been reviewed and is approved for publication.

FOR THE COMMANDER

A handwritten signature in cursive script that reads "Thomas J. Alpert". The signature is written in dark ink on a light background.

Thomas J. Alpert, Major, USAF
Chief, ESD Lincoln Laboratory Project Office

Non-Lincoln Recipients

PLEASE DO NOT RETURN

Permission is given to destroy this document
when it is no longer needed.

MASSACHUSETTS INSTITUTE OF TECHNOLOGY
LINCOLN LABORATORY

SOLID STATE RESEARCH

QUARTERLY TECHNICAL REPORT

1 NOVEMBER 1984 — 31 JANUARY 1985

ISSUED 14 JUNE 1985

Approved for public release; distribution unlimited.

LEXINGTON

MASSACHUSETTS

ABSTRACT

This report covers in detail the solid state research work of the Solid State Division at Lincoln Laboratory for the period 1 November 1984 through 31 January 1985. The topics covered are Solid State Device Research, Quantum Electronics, Materials Research, Microelectronics, and Analog Device Technology. Funding is primarily provided by the Air Force, with additional support provided by the Army, DARPA, Navy, NASA, and DOE.

TABLE OF CONTENTS

Abstract	iii
List of Illustrations	vii
Introduction	xi
Reports on Solid State Research	xiii
Organization	xxi
1. SOLID STATE DEVICE RESEARCH	1
1.1 Heterodyne Radiometry at 28 μm	1
1.2 Wideband Integrated-Optics Electrooptic Intensity Modulator for 3.39- μm Operation	6
2. QUANTUM ELECTRONICS	13
2.1 Transient Carrier Density and Light Output Measurements of Pulsed Diode Lasers	13
3. MATERIALS RESEARCH	17
3.1 Zone-Melting Recrystallization of Si- and Ge-on-Insulator Films	17
3.2 MOSFETs Fabricated Using Self-Aligned Silicide Technology	22
3.3 GaAs Optical MESFET Detectors Fabricated on a Monolithic GaAs/Si Substrate	26
4. MICROELECTRONICS	31
4.1 A 420 \times 420 CCD Imager for Ground-Based Satellite Surveillance	31
4.2 SAW/FET Wideband Programmable Filter	34
4.3 Etched-Emitter Silicon PBT	36
4.4 Linewidth Control with Masked Ion-Beam Lithography Using Stencil Masks	41
4.5 Solid-State Submillimeter Heterodyne Radiometer	44
4.6 Persistent Photoconductivity in Quantum Well Resonators	47
5. ANALOG DEVICE TECHNOLOGY	51
5.1 <i>In situ</i> Amplitude and Phase Adjustment of SAW Devices by Laser-Photochemical Etching	51
5.2 Superconductive Chirp-Transform Spectrum Analyzer	55

LIST OF ILLUSTRATIONS

Figure No.		Page
1-1	Schematic Diagram of a 28- μm Infrared Heterodyne Spectrometer Containing a PbSnSe Diode Laser Local Oscillator and a HgCdTe Photomixer, Both Cooled to About 20 K	2
1-2	Photocurrent and RF Noise Detected by a HgCdTe Photodiode Mixer as a Function of Current into the PbSnSe Diode Laser Local Oscillator	3
1-3	Current-Voltage Characteristics of HgCdTe Photodiode Mixer in the Dark and Illuminated with a 50- μW , 28- μm Local Oscillator Beam	4
1-4	Synchronously Detected 28- μm Heterodyne Signal as a Function of Time with a 400°C Blackbody Off and On the Detector	5
1-5	Schematic of Guided-Wave Mach-Zehnder Interferometric Modulator with Center-Tapped Electrode. The Two Y Junctions have 2° Full Branching Angles, and the Direction of Optical Propagation (Except at These Bends) Is in the y -Direction. The 1- μm -Thick Cr/Au Electrodes Are 0.8 cm Long and Are Fabricated on a 2000-Å-Thick SiO ₂ Buffer Layer. The Interferometer Arms Are 1.8 cm Long and Are Separated by 100 μm	6
1-6	Top Trace Is 70-V Peak-to-Peak Sinusoid Used as the Modulator Drive Signal. Bottom Trace Is Modulator Output. Modulator Was DC-Biased to Its Half Intensity Point with 15.5 V ($V_{\pi}/2$). Two π Phase Flips Are Seen	7
1-7	Linear Small-Signal Frequency Response of Modulator. x's Are Measured Response. Solid Line Is Predicted by RLC Equivalent Circuit	8
1-8	p-Column JFET (a) Top View; (b) Gate Cross Section A-A	9
1-9	Characteristic Curves for a 4- μm p-Column JFET	10
2-1	Measured Carrier Density C and Light Output L as a Function of Time for DC Bias Currents of (a) 79 mA, (b) 72 mA, (c) 66 mA, and (d) 61 mA. Dotted Line in Each Box Represents the Estimated Carrier Density at Threshold. There Is No Light Output Curve for Case (d) Since the Diode Was Below Threshold	14
3-1	Optical Micrographs of (a) Branched and (b) Unbranched Subboundaries in Recrystallized SOI Films	17
3-2	Regions of Branched and Unbranched Subboundaries as a Function of Si and SiO ₂ Thickness	18
3-3	Optical Micrograph of a Recrystallized Film Showing Unbranched Subboundaries and Other Less Extended Defects	19

Figure No.		Page
3-4	Interference Patterns with a 4- μm /Fringe Sensitivity for 3-in. (a) Bare Si Wafer and (b) Recrystallized SOI Wafer	19
3-5	(a) Seeded Ge-on-Insulator Sample Structure and (b) Optical Micrographs of Ge-on-Insulator Wafers After ZMR with Seed and Scan Parallel to $\langle 100 \rangle$ and $\langle 110 \rangle$ Directions	20
3-6	Nomarski Micrographs of Seeded 50- μm Ge-on-Insulator Islands After ZMR and Defect Etching	21
3-7	Scanning Electron Micrograph of Seeded 50- μm Ge-on-Insulator Islands After ZMR	
3-8	Process Sequence for MOSFETs Fabricated Using Self-Aligned Silicide Technology	23
3-9	Scanning Electron Micrograph of MOSFET Surface After Removal of W by Selective Etching	24
3-10	Gate-Source (Gate-Drain) Characteristic of n-Channel MOSFET	25
3-11	Transistor Characteristics of (a) n-Channel and (b) p-Channel MOSFETs	25
3-12	Schematic Diagram of Circuit Used to Bias Packaged OPFETs	27
3-13	Pulse Response of Packaged OPFET for Gate Bias Values (from Top to Bottom) of -1.0, -1.25, and -1.5 V	28
3-14	Fastest Pulse Response Obtained for a Packaged OPFET (Gate Bias Is -1.4 V)	29
4-1	Schematic Diagram of the 420 \times 420 Pixel CCD Imager	31
4-2	Photograph of the 420 \times 420 CCD Imager Together with Detailed Views of the Upper Left Corner and the Output Detection Circuit in the Lower Right	32
4-3	Monitor Photo Showing the Output Signal Resulting from an Image Projected onto the CCD	33
4-4	Photomicrograph of the SAW/FET Chip Containing Dual 175-Tap Sampling Arrays. Chip Size Is 6.5 \times 4.9 mm	34
4-5	Magnified View of Figure 4-4 Showing the Lower Left Corner. The Taps Are on a 30- μm Pitch	35
4-6	Schematic Diagram of One Stage of the Programming Circuit	36

Figure No.		Page
4-7	Three PBT Configurations: (a) Encapsulated-Base, (b) Etched-Collector, and (c) Etched-Emitter. The Base Grating Periodicity and Metal Thickness Are $4d$ and L , Respectively	37
4-8	The Unity Short-Circuit Current-Gain Frequency f_T as a Function of V_{BE} for the Three Devices of Figure 4-7	38
4-9	Comparison of the Extent of the Depletion Region Surrounding Both the Intrinsic and Extrinsic Base Regions of the Device when Biased as an Etched-Collector or Etched-Emitter PBT	39
4-10	Common Emitter Current-Gain vs Frequency for the Best Etched-Emitter and Etched-Collector Devices	40
4-11	(a) Calculation of Image Intensity of an Optical Exposure System Operating at a Wavelength of 436 nm and with a 0.28 NA Lens. The Ideal Image Is Three $0.75\text{-}\mu\text{m}$ -Wide Lines Spaced $0.75\ \mu\text{m}$ Apart. The Data for This Graph Were Taken from Figures 3 and 4 of Reference 6. (b) Image Intensity Obtained when Exposing $0.65\text{-}\mu\text{m}$ -Wide Lines on $2\text{-}\mu\text{m}$ Centers with Masked Ion-Beam Lithography Using a Stencil Mask. The Only Deviation from the Ideal Image Is a Background Exposure Level of Approximately 3 Percent, and Slight Taper (Imperceptible on Graph) of the Line Edges	42
4-12	Plot of Measured Linewidths for $2.35\text{-}\mu\text{m}$ - and $0.65\text{-}\mu\text{m}$ -Wide Lines. The Dots Are Data Points Obtained from Measuring SEM Micrographs and the Triangles Are Data Points Taken with the Optical Linewidth Measuring Instrument	43
4-13	Block Diagram of 557-GHz Heterodyne Radiometer	44
4-14	Absorption Line of H_2O Jet Illuminated by Hg Arc Lamp Under Conditions Which Caused a Self Reversal Around the Center of the Line	45
4-15	Electron Energy as a Function of Position in a Quantum Well Structure with Positive Charge in the Barriers and the Electrons Outside the Barrier Well Region. The Dashed Lines Show the Conduction Band in the Absence of Ionized Centers	46
4-16	Observed (a) and Calculated (b) I-V Curves for the Structure Shown in Figure 4-15 for Several Exposures to $0.85\text{-}\mu\text{m}$ Radiation. The Long-Dashed Curve Is Unexposed, the Solid Curve Has Had an Arbitrary Exposure Q , the Short-Dashed Curve Has Exposure $10 Q$, and the Broken Curve Has Exposure $100 Q$	48

Figure No.		Page
5-1	Laser Microchemically Etched Test Delay-Line Structures Demonstrate Monotonic Change in (a) Phase and (b) Amplitude Response. The Mo Film Between the Delay-Line Transducers Is Continuously Removed in a Raster Scan Fashion to Uncover 0.25- μ m Strips of (a) LiNbO ₃ for Phase Compensation and (b) Cermet for Amplitude Compensation	52
5-2	(a) Amplitude Response and (b) Phase Deviations from Quadratic Response of the Fully Compensated RAC Compared with the Initial Uncompensated Device Measurements and the Target Levels. The Coupled Amplitude/Phase Error at the Low-Frequency Band-Edge in the Response Measurements of the Compensated RAC Is the Result of a Large and Inappropriate Local Amplitude Correction	54
5-3	Chirp Filter Formed by Cascading Backward-Wave Couplers Between Adjacent Electromagnetic Delay Lines	56
5-4	Chirp-Transform Spectrum Analyzer Employing Superconductive Expander and Compressor. Frequency-Time Plots Are Shown for Various Points in the Signal Path. The RF Signal Input Shown Is an Example of the Possible Signals Within the $f_o - B/2$ to $f_o + B/2$ Analyzer Input Band; in This Case Three Tones Are Shown, One at f_o , a Second at $f_o - B/2$, and a Third at $f_o + B/2$. These Are Mapped by the Analyzer into Time Slots Spaced by $T_c/2$	57
5-5	Multiple Exposure of Sampling-Scope Output for Successive Single-Tone Inputs of 4000 MHz (Leftmost Pulse) to 3400 MHz (Rightmost Pulse) in 100-MHz Increments. The Input Power Level Is -7 dBm	58

INTRODUCTION

1. SOLID STATE DEVICE RESEARCH

An infrared heterodyne spectrometer has been constructed which operates at $28\ \mu\text{m}$ using a PbSnSe diode laser local oscillator and a HgCdTe photodiode photomixer, both cryogenically cooled to about 20 K. In spite of low power and excess noise of the diode laser and weak rectification characteristics of the photodiode, a heterodyne NEP of $3.5 \times 10^{-19}\ \text{W/Hz}$ was measured over a bandwidth of 500 MHz. This is the lowest wide-bandwidth NEP achieved to date in this long-wavelength region.

A LiNbO₃ guided-wave interferometric modulator has been demonstrated at $\lambda = 3.39\ \mu\text{m}$ with a linear small-signal 3-dB bandwidth of 1.8 GHz and an extinction ratio of 18.9 dB. This is the first such modulator for $\lambda > 1.6\ \mu\text{m}$.

InP junction field effect transistors have been fabricated which exhibit a unity power gain frequency of 7 GHz. A periodic array of p⁺ columns implanted through an n-type channel is used to form the active gate region of the device. This is the first fully implanted structure in InP; it should offer several advantages over more complicated JFETs.

2. QUANTUM ELECTRONICS

The time-dependent carrier density and light output of a diode laser excited by short current pulses and a DC bias were measured with picosecond time resolution using a mode-locked dye laser and a new beat-frequency sampling technique. At below-threshold DC bias currents, the carrier lifetime was determined from the exponential carrier density decay. At higher biases, strong gain depletion was observed as the diode laser emitted short light pulses.

3. MATERIALS RESEARCH

Major advances have been achieved in the effort to eliminate sub-grain boundaries from Si-on-insulator films prepared by zone-melting recrystallization (ZMR), and the warp of ZMR wafers has been significantly reduced. Promising results have been obtained in initial experiments on the use of ZMR to prepare single-crystal Ge films on SiO₂-coated Si substrates.

n- and p-channel MOSFETs with self-aligned WSi₂ gate, source, and drain have been fabricated by using a technique reported earlier, which employs ion-beam mixing and rapid thermal annealing to form smooth WSi₂ films on patterned SiO₂-coated Si substrates and simultaneously to form shallow p-n junctions. The device characteristics obtained indicate that this technique should be useful in the fabrication of CMOS integrated circuits.

Optical MESFETs have been fabricated in a GaAs layer grown by molecular beam epitaxy directly on a Si wafer. These devices, the first high-speed detectors fabricated on a monolithic GaAs/Si substrate, have shown rise times as low as 5 ns in response to pulses with 2 mW peak power from a diode laser emitting at 840 nm.

4. MICROELECTRONICS

A 420×420 pixel CCD imager has been designed and fabricated for the GEODSS program. The front-illuminated polysilicon gate device is 11.3×11.3 mm, and is designed to be abutted to two other identical dies on two adjacent sides. Initial wafer runs have yielded several imagers exhibiting excellent performance with very low defect levels (regions of high dark current).

A silicon integrated circuit has been designed and fabricated to work in conjunction with a SAW device, producing a programmable transversal filter with 50-MHz bandwidth. The silicon chip is nMOS, 6.5×4.9 mm in size, and uses relaxed design rules and dynamic circuitry.

Silicon permeable-base transistors have been fabricated which exhibit a small-signal short-circuit unity-current-gain frequency, f_T , over 20 GHz. This compares favorably with device results using the most advanced high-speed silicon technologies, including submicrometer gatelength MOSFETs and super self-aligned bipolar transistors.

The large process latitude and excellent linewidth control possible with masked ion beam lithography has been demonstrated by employing stencil masks. Submicrometer exposures in polymethylmethacrylate resist exhibit linewidth variation within measurement error ($<500 \text{ \AA}$) for a change in exposing dose over an order of magnitude.

A compact solid state radiometer operating at 557 GHz ($540 \mu\text{m}$) has been developed to obtain the absorption spectrum of H_2O in a water vapor jet expanding adiabatically into a high-vacuum chamber. The receiver had a noise temperature of 8000 K (DSB) and a frequency resolution of approximately 600 kHz. With a power consumption of 3 W and a weight of 3 kg, the radiometer can be used for space-based applications.

The first observation of persistent photoconductivity in resonant tunneling structures has been made. This effect has been useful in investigating the charge distribution and electric fields near the heterojunction interface and in uniquely determining the barrier parameters. The model employed should help in the design and fabrication of optimized resonant tunneling devices.

5. ANALOG DEVICE TECHNOLOGY

Convolution of an image with an electronically controllable Gaussian kernel function has been carried out in the focal plane of a large CCD imager operating with standard television timing. Off-chip subtraction of the Gaussian-convolved images and subsequent thresholding were used to perform edge extraction in real time using the difference-of-Gaussians algorithm.

Laser photochemical etching has been applied to the trimming of metallic phase-compensating and metal/cermet amplitude-compensating films on surface-acoustic-wave devices. Adjustment of phase in 0.15° increments and amplitude in 0.01-dB increments has been demonstrated. When controlled by phase and amplitude measurements in a closed loop, this *in situ* technique is expected to result in devices with an order-of-magnitude accuracy improvement.

Spectral analysis over an instantaneous bandwidth of 2.4 GHz has been demonstrated utilizing superconductive dispersive delay lines in a chirp-transform configuration. A two-tone resolution of 43 MHz and ± 1.2 -dB amplitude uniformity were achieved.

REPORTS ON SOLID STATE RESEARCH

1 November 1984 through 31 January 1985

PUBLISHED REPORTS

Journal Articles

JA No.

- | | | | |
|------|---|--|---|
| 5557 | Spatial-Resolution Limits of Laser Patterning: Submicrometer Projection Microchemistry | D.J. Ehrlich
J.Y. Tsao | In <i>Laser-Controlled Chemical Processing of Surfaces</i> , edited by A.W. Johnson, D.J. Ehrlich, and H.R. Schlossberg (North-Holland, New York, 1984), p. 195 |
| 5584 | UV-Laser Photodeposition from Surface-Adsorbed Mixtures of Trimethylaluminum and Titanium Tetrachloride | J.Y. Tsao
D.J. Ehrlich | J. Chem. Phys. 81 , 4620 (1984) |
| 5613 | Experimental Test of Open-Loop Maximum-Power-Point Tracking Techniques for Photovoltaic Arrays | G.W. Hart*
H.M. Branz
C.H. Cox III | Solar Cells 13 , 185 (1984) |
| 5623 | Advances in LEC Growth of InP Crystals | G.W. Iseler | J. Electron. Mater. 13 , 989 (1984) |
| 5635 | Traveling-Wave Electro-optic Modulator with Maximum Bandwidth-Length Product | R.A. Becker | Appl. Phys. Lett. 45 , 1168 (1984) |
| 5648 | A High Frequency GaAs Optical Guided-Wave Electro-optic Interferometric Modulator | J.P. Donnelly
N.L. DeMeo
G.A. Ferrante
K.B. Nichols | IEEE J. Quantum Electron. QE-21 , 18 (1985) |

* Author not at Lincoln Laboratory.

JA No.

- | | | | |
|------|--|---|--|
| 5652 | Merged CMOS/Bipolar Technologies Utilizing Zone-Melting-Recrystallized SOI Films | B-Y. Tsaur
R.W. Mountain
C.K. Chen
J.C.C. Fan | IEEE Electron Device Lett. EDL-5 , 461 (1984) |
| 5654 | Donor Identification in Liquid Phase Epitaxial Indium Phosphide | M.S. Skolnick*
P.J. Dean*
S.H. Groves
E. Kuphal* | Appl. Phys. Lett. 45 , 962 (1984) |
| 5656 | Metal-Semiconductor Field-Effect Transistors Fabricated in GaAs Layers Grown Directly on Si Substrates by Molecular Beam Epitaxy | G.M. Metzger
H.K. Choi
B-Y. Tsaur | Appl Phys. Lett. 45 , 1107 (1984) |
| 5658 | Long-Term Prospects for Lasers in Microfabrication | D.J. Ehrlich | Editorial, Laser Focus 20 , 108 (1984) |
| 5660 | Masked Ion Beam Resist Exposure Using Grid Support Stencil Masks | J.N. Randall
D.C. Flanders
N.P. Economou
J.P. Donnelly
E.I. Bromley | J. Vac. Sci. Technol. 3 , 58 (1985) |
| 5665 | Error Reduction in Laser Remote Sensing: Combined Effects of Cross-Correlation and Signal Averaging | N. Menyuk
D.K. Killinger
C.R. Menyuk* | Appl. Opt. 24 , 118 (1985) |
| 5676 | Quantum Well Oscillators | T.C.L.G. Sollner
P.E. Tannenwald
D.D. Peck
W.D. Goodhue | Appl. Phys. Lett. 45 , 1319 (1984) |
| 5687 | High Resistivity InGaAs(Fe) Grown by a Liquid Phase Epitaxial Substrate-Transfer Technique | S.H. Groves
V. Diadiuk
M.C. Plonko
D.L. Hovey | Appl. Phys. Lett. 46 , 78 (1985) |

* Author not at Lincoln Laboratory.

JA No.

- | | | | |
|------|---|--|---|
| 5688 | Lateral Photodetectors on Semi-insulating InGaAs and InP | V. Diadiuk
S.H. Groves | Appl. Phys. Lett. 46 ,
157 (1985) |
| 5691 | Microwave Operation of Sub-micrometer Channel-Length Silicon MOSFETs | D.C. Shaver | IEEE Electron Device Lett. EDL-6 , 36 (1985) |
| 5696 | Surface-Emitting GaInAsP/InP Laser with Low Threshold Current and High Efficiency | Z.L. Liao
J.N. Walpole | Appl. Phys. Lett. 46 ,
115 (1985) |
| 5701 | Planar GaAs p-i-n Photodiode with Picosecond Time Response | W. Lenth
A. Chu
L.J. Mahoney
R.W. McClelland
R.W. Mountain
D.J. Silversmith | Appl. Phys. Lett. 46 ,
191 (1985) |
| 5703 | A Novel GaInAsP/InP Distributed Feedback Laser | Z.L. Liao
D.C. Flanders
J.N. Walpole
N.L. DeMeo | Appl. Phys. Lett. 46 ,
221 (1985) |

Meeting Speeches**MS No.**

- | | | | |
|-------|--|---------------|---|
| 5899A | Raman Scattering as a Probe of Thin Films | S.R.J. Brueck | <i>Proceedings of DARPA Workshops on Diamond-Like Carbon Coatings</i> , edited by B. Bendow (The BDM Corporation, Albuquerque, New Mexico, 1983), p. 214 |
| 6380 | Recent Advances in Solid-State Laser Materials | P.F. Moulton | <i>In Defect Properties and Processing of High-Technology Nonmetallic Materials</i> , edited by J. H. Crawford, Jr., Y. Chen, and W.A. Sibley (North-Holland, New York, 1984), p. 393 |

MS No.

- | | | | |
|-------|--|---|---|
| 6382 | Electromagnetically-Induced Surface Microstructures and Enhanced Field Effects in Laser Processing | S.R.J. Brueck
D.J. Ehrlich
D.V. Murphy
J.Y. Tsao | In <i>Laser-Controlled Chemical Processing of Surfaces</i> , edited by A.W. Johnson, D.J. Ehrlich, and H.R. Schlossberg (North-Holland, New York, 1984), p. 295 |
| 6397 | UV Laser-Initiated Deposition of Al ₂ O ₃ Films: The Effect of Surface Irradiation | T.F. Deutsch
D.J. Silversmith
R.W. Mountain | In <i>Laser-Controlled Chemical Processing of Surfaces</i> , edited by A.W. Johnson, D.J. Ehrlich, and H.R. Schlossberg (North-Holland, New York, 1984), p. 67 |
| 6400 | Recent Advances in UV Laser Photodeposition | J.Y. Tsao
D.J. Ehrlich | In <i>Laser-Controlled Chemical Processing of Surfaces</i> , edited by A.W. Johnson, D.J. Ehrlich, and H.R. Schlossberg (North-Holland, New York, 1984), p. 115 |
| 6400A | Laser-Chemical Modification of Nucleation Barriers for Area-Selective Thin Film Growth | J.Y. Tsao
D.J. Ehrlich | J. Cryst. Growth 68 , 176 (1984) |
| 6654 | Guided-Wave Optics in LiNbO ₃ : Physical Properties, Devices and Signal Processing Systems | R.A. Becker | <i>Integrated Optical Circuit Engineering</i> , Proc. SPIE 517 , 194 (1984) |
| 6661 | Radiation-Field Coupling in Optical Waveguide Structures with Closely Spaced Abrupt Bends and Branches | D. Yap
L.M. Johnson | <i>Integrated Optical Circuit Engineering</i> , Proc. SPIE 517 , 137 (1984) |
| 6750 | Direct Patterning by Laser Microchemistry | D.J. Ehrlich | Proc. Intl. Dry Processing Symp., Tokyo, Japan, 10-12 October 1984, edited by K. Nishizawa, p. 72 |

UNPUBLISHED REPORTS

Journal Articles

JA No.

5594	Surface Acoustic Wave Devices	D.E. Oates	Accepted as Chapter 8 in <i>VLSI Electronics: Micro- structure Science</i> , Vol. 9, N. Einspruch, Ed. (Academic Press, New York, 1985)
5695	Laser-Microchemical Reactions for Maskless Device Processing: Surface Modifications for Selected-Area Growth	D.J. Ehrlich J.Y. Tsao	Accepted by <i>J. Vac. Sci. Technol.</i>
5722	Wide-Bandwidth Guided-Wave Electrooptic Intensity Modulator at $\lambda = 3.39 \mu\text{m}$	R.A. Becker R.H. Rediker T.A. Lind	Accepted by <i>Appl. Phys. Lett.</i>

Meeting Speeches*

MS No.

6078F	Microstructure Electromagnetic Effects in Laser-Material Interactions	S.R.J. Brueck	Seminar, Electrical Engi- neering Dept., Washington University, St. Louis, Missouri, 14 December 1984
6523A	Wideband Electrooptic Analog-to- Digital Converters	R.A. Becker C.E. Woodward F.J. Leonberger	} GOMAC 1984 (Govt. Microcircuits Applications Conference), Las Vegas, Nevada, 6-8 November 1984
6627	Millimeter-Wave Monolithic Circuits for Receiver and Transmitter Applications	A. Chu B.J. Clifton R.A. Murphy R.W. Sudbury	

* Titles of Meeting Speeches are listed for information only. No copies are available for distribution.

MS No.

6549A	10.6- μ m Photomixer Arrays at 195 K	D.L. Spears	1985 Mtg., IRIS Specialty Group on Active Systems, Laurel, Maryland, 14 November 1984
6700	Chemically Amplified Laser Direct Writing of Aluminum	J.Y. Tsao D.J. Ehrlich	Materials Research Society Mtg., Boston, 26-30 November 1984
6713	Recent Developments in the Methods and Applications of Reactive Laser-Direct-Patterning Techniques	D.J. Ehrlich J.Y. Tsao	
6718	Characterization, Control and Elimination of Subboundaries in Silicon on Insulators	M.W. Geis C.K. Chen H.I. Smith* R.W. Mountain C.L. Doherty	
6719	Applications of Transient Heating for Semiconductor Material and Device Processing	J.C.C. Fan	
6720	SOI Technologies: Device Applications and Future Prospects	B-Y. Tsaur	
6722	Recent Advances in Si and Ge Zone-Melting Recrystallization	C.K. Chen M.W. Geis H.K. Choi B-Y. Tsaur J.C.C. Fan	
6745	Laser Diagnostics of Semiconductor Fabrication Processes and Devices	S.R.J. Brueck	
6702	Wide-Band SAW/FET Programmable Transversal Filter	D.E. Oates D.L. Smythe R.W. Ralston A.C. Anderson J.B. Green	1984 IEEE Ultrasonics Symp., Dallas, Texas, 14-16 November 1984

* Author not at Lincoln Laboratory.

MS No.

6707	Application of Laser Direct-Write Processes to Trimming of SAW Devices	V.S. Dolat D.J. Ehrlich J.Y. Tsao	} 1984 IEEE Ultrasonics Symp., Dallas, Texas, 14-16 November 1984
6708	Application of SAW Convolver to Spread Spectrum Communication	J.H. Cafarella	
6709	Holographic-Grating Acoustic Devices	P.G. Gottschalk D.E. Oates P.V. Wright	
6712	Wideband Radar Signal Processor Based on SAW Convolver	I. Yao E.M. Hauser C.A. Bouman G.T. Flynn J.H. Cafarella	
6731	Merged CMOS/Bipolar Technologies and Microwave MESFETs Utilizing Zone-Melting-Recrystallized SOI Films	B-Y Tsaor H.K. Choi C.K. Chen C.L. Chen R.W. Mountain J.C.C. Fan	Intl. Electron Devices Mtg. (IEDM), San Francisco, 9-12 December 1984
6732A	Optical Techniques for Processing of Electrical Signals	R.C. Williamson	Seminar, Electrical Engineering Dept., Howard University, Washington, DC, 4 December 1984
6792	Application of Coherent LIDAR to Remote Sensing of Atmospheric Species	D.K. Killinger N. Menyuk	OSA Topical Meeting on Optical Remote Sensing of the Atmosphere, Lake Tahoe, Nevada, 15-18 January 1985
6801	Organometallic Chemical Vapor Deposition of GaAs/AlGaAs and its Application to Photovoltaics	R.P. Gale	New England Section, American Association for Crystal Growth, Cambridge, Massachusetts, 28 November 1984

MS No.

6804	UV-Laser Photodeposition of Patterned Catalyst Films from Adsorbate Mixtures	D.J. Ehrlich J.Y. Tsao	OSA Topical Meeting on Microphysics of Surfaces, Beams and Adsorbates, Santa Fe, New Mexico, 4-6 February 1985
6810	Laser-Microchemical Reactions for Maskless Device Processing	D.J. Ehrlich J.Y. Tsao	National AVS Symp., Reno, Nevada, 4-7 December 1984

ORGANIZATION

SOLID STATE DIVISION

A.L. McWhorter, *Head*
I. Melngailis, *Associate Head*
E. Stern, *Associate Head*
J.F. Goodwin, *Assistant*

P.E. Tannenwald, *Senior Staff*

QUANTUM ELECTRONICS

A. Mooradian, *Leader*
P.L. Kelley, *Associate Leader*

Barch, W.E.	Harrison, J.*
Belanger, L.J.	Johnson, B.C.*
Brueck, S.R.J.	Killinger, D.K.
Burke, J.W.	Menyuk, N.
Bushee, J.F., Jr.	Moulton, P.F.
DeFeo, W.E.	Sharpe, K.A.
Feldman, B.	
Hancock, R.C.	

ELECTRONIC MATERIALS

A.J. Strauss, *Leader*
J.C.C. Fan, *Associate Leader*
H.J. Zeiger, *Senior Staff*

Anderson, C.H., Jr.	Krohn, L., Jr.
Button, M.J.	Mastromattei, E.L.
Chen, C.K.	McClelland, R.W.
Choi, H.K.	Metze, G.M.
Connors, M.K.	Nitishin, P.M.
Delaney, E.J.	Pantano, J.V.
Fahey, R.E.	Tracy, D.M.
Finn, M.C.	Tsaur, B-Y.
Gale, R.P.	Turner, G.W.
Iseler, G.W.	Wang, C.A.
King, B.D.	Windhorn, T.H.
Kolesar, D.F.	

APPLIED PHYSICS

R.C. Williamson, *Leader*
D.L. Spears, *Assistant Leader*
T.C. Harman, *Senior Staff*
R.H. Rediker, *Senior Staff*

Anderson, K.K.*	Groves, S.H.	Plonko, M.C.
Becker, R.A.	Hovey, D.L.	Reeder, R.E.
Cox, C.H., III	Johnson, L.M.	Schloss, R.P.*
DeMeo, N.L., Jr.	Liau, Z.L.	Tsang, D.Z.
Diadiuk, V.	Lind, T.A.	Walpole, J.N.
Donnelly, J.P.	McBride, W.F.	Whitaker, N.*
Duffy, P.E.	Molter, L.A.*	Woodhouse, J.D.
Ferrante, G.A.	O'Donnell, F.J.	Yap, D.*

* Research Assistant

† Part Time

ANALOG DEVICE TECHNOLOGY

R.W. Ralston, *Leader*

R.S. Withers, *Assistant Leader*

Anderson, A.C.
Arsenault, D.R.
Boisvert, R.R.
Bouman, C.A.
Brogan, W.T.
Delaney, M.*
Dolat, V.S.
Fischer, J.H.

Fitch, G.L.
Flynn, G.T.
Green, J.B.
Hauser, E.M.
Holtham, J.H.
Kernan, W.C.
Lattes, A.L.
Macedo, E.M., Jr.

Macropoulos, W.
Marden, J.A.
Melngailis, J.†
Oates, D.E.
Sage, J.P.
Thompson, K.E.‡
Yao, I.

MICROELECTRONICS

W.T. Lindley, *Leader*

D.J. Ehrlich, *Assistant Leader*

B.B. Kosicki, *Assistant Leader*

R.A. Murphy, *Assistant Leader*

Astolfi, D.K.
Black, J.G.
Bozler, C.O.
Burke, B.E.
Burke, J.W.
Calawa, A.R.
Chen, C.L.
Chiang, A.M.
Clifton, B.J.
Correa, C.A.
Daniels, P.J.
Durant, G.L.
Efremow, N.N., Jr.
Felton, B.J.
Geis, M.W.

Goodhue, W.D.
Gray, R.V.
Hollis, M.A.
Lax, B.†
LeCoz, Y.L.*
Lincoln, G.A., Jr.
Lyszczarz, T.M.
Mahoney, L.J.
Manfra, M.J.
McGonagle, W.H.
Mountain, R.W.
Nichols, K.B.
Pang, S.W.
Parker, C.D.
Piacentini, W.J.

Pichler, H.H.
Rabe, S.
Randall, J.N.
Rathman, D.D.
Reinold, J.H.
Rothschild, M.
Sedlacek, J.H.C.
Silversmith, D.J.
Smythe, D.L., Jr.
Sollner, T.C.L.G.
Sullivan, D.J.
Taylor, J.A.*
Vera, A.
Wilde, R.E.

* Research Assistant

† Part Time

‡ Staff Associate

1. SOLID STATE DEVICE RESEARCH

1.1 HETERODYNE RADIOMETRY AT 28 μm

High-resolution heterodyne radiometry at 28 μm is of considerable interest in the field of astrophysics because of the strong optical transition of molecular hydrogen at 28 μm and the increased spectral intensity of blackbody sources at long wavelengths.¹ We have constructed and tested the first infrared heterodyne spectrometer operating at 28 μm , which uses a PbSnSe diode laser local oscillator and a HgCdTe photodiode photomixer (both cryogenically cooled to about 20 K). In spite of low power and excess noise of the diode laser and weak rectification characteristics of the photodiode, a heterodyne NEP of 3.5×10^{-19} W/Hz was measured over a bandwidth of 500 MHz. This is the lowest wideband NEP achieved to date in this long-wavelength region.

Figure 1-1 is a schematic diagram of the infrared heterodyne spectrometer. The diode laser (DL) and photomixer (P) are mounted on a copper cold stage which is thermally attached to a closed-cycle cooler (CC) by means of flexible copper braid in order to de-couple cooler vibrations, and which is mechanically attached to the base of the vacuum chamber by means of a perforated nylon post with low thermal conductance. The strongly divergent laser radiation is collimated with an $f/1.8$ 60°-off-axis parabolic collection mirror (CM), reflected from two plane mirrors (M) and an uncoated silicon beam splitter (BS), and imaged onto the detector with a matched off-axis parabolic focusing mirror (FM). Thermal radiation enters the vacuum chamber through a CsI window and mixes with the laser radiation at the beam splitter. In the local-oscillator-starved receiver limit the performance of the uncoated silicon (30 percent first-surface reflectivity and 49 percent single-pass transmission) is about 60 percent of that of the optimum 50/50 beam splitter, which has yet to be developed at 28 μm . The beam was imaged onto the detector at an angle 20° off normal to avoid feedback to the laser. The entire optical system was designed so as to minimize any chance of feedback, which gives rise to high-frequency instabilities in diode lasers.

The 28- μm PbSnSe diode lasers (developed for NASA by Laser Analytics Inc.²) were evaluated as local oscillators by measuring the photocurrent produced in the photomixer and the RF noise associated with the laser power. Typical data are presented in Figure 1-2, which shows photocurrent and RF noise (in the 1 to 100 MHz band) as a function of current into the diode laser. The threshold current of this broad-area ($250 \times 250 \mu\text{m}$) PbSnSe laser was about 1.1 A at 20.6 K. At 28 μm the HgCdTe photodiode^{3,4} had a current responsivity of about $9 \mu\text{A}/\mu\text{W}$, which corresponds to 40 percent quantum efficiency. Thus the peak photocurrent of 550 μA corresponds to a detected laser power of about 60 μW , which is much less than the output power (about 450 μW) of the PbSnSe laser. The large power loss was due to a combination of incomplete collection with the $f/1.8$ mirrors, low beam splitter reflectivity (30 percent), and the image size ($200 \times 250 \mu\text{m}$) being larger than the detector size ($180 \times 190 \mu\text{m}$).

With laser radiation on the photomixer the RF noise level increased in an erratic fashion, and at times it was over an order of magnitude above the dark level due primarily to the noise

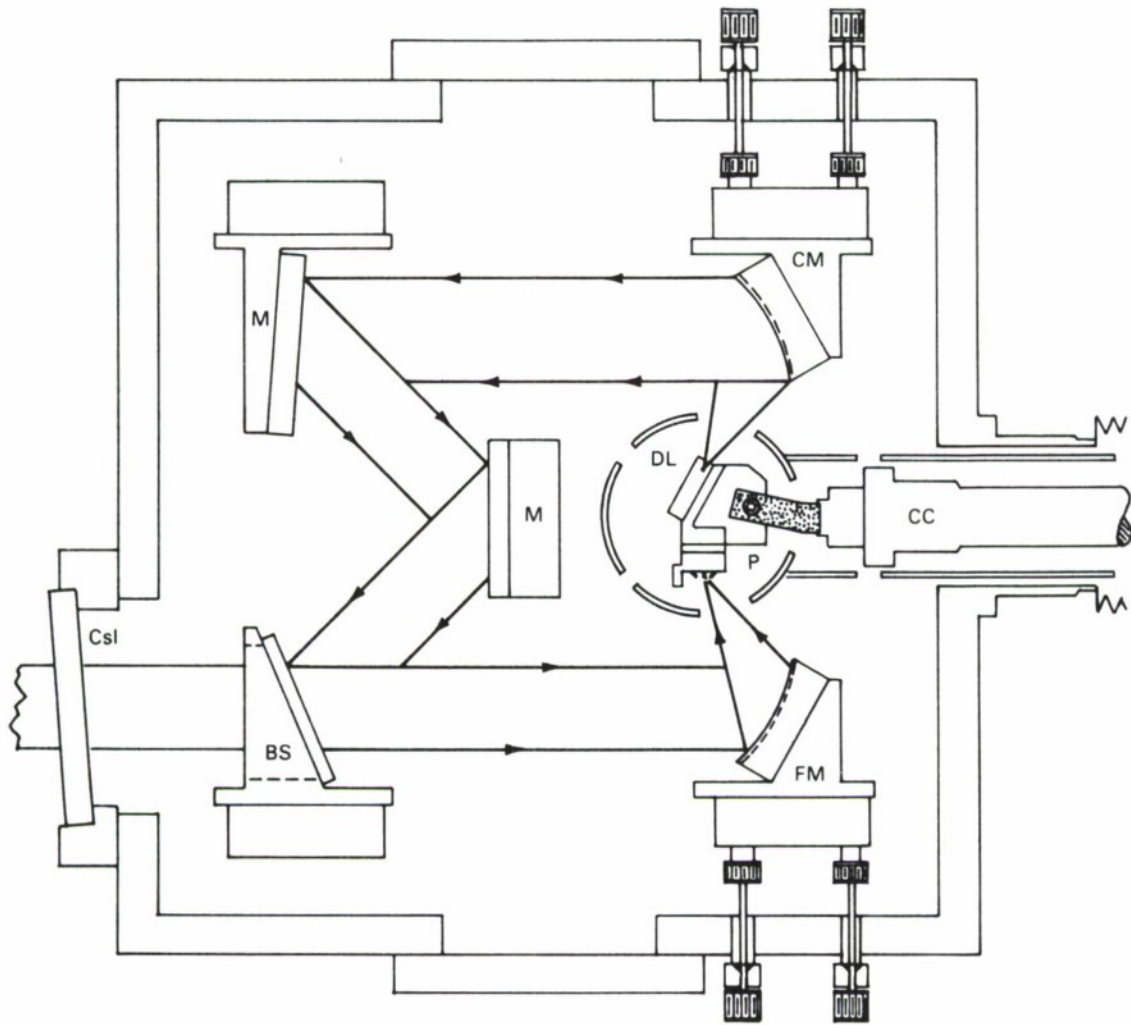


Figure 1-1. Schematic diagram of a 28- μm infrared heterodyne spectrometer containing a PbSnSe diode laser local oscillator and a HgCdTe photomixer, both cooled to about 20 K.

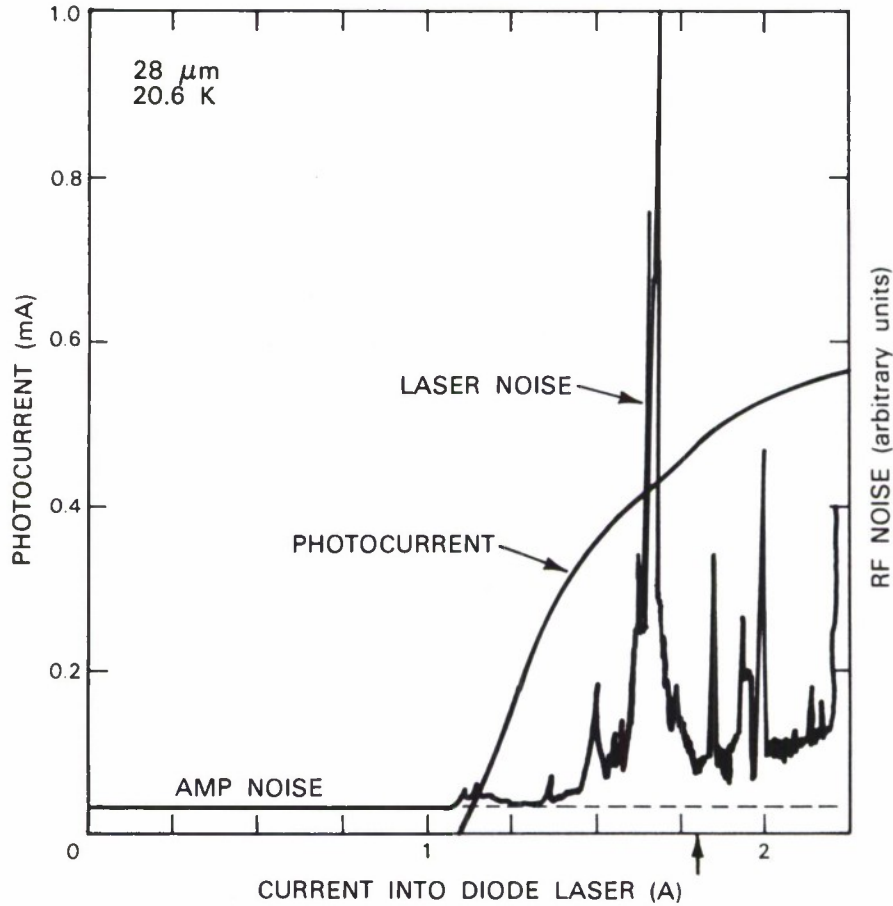


Figure 1-2. Photocurrent and RF noise detected by a HgCdTe photodiode mixer as a function of current into the PbSnSe diode laser local oscillator.

of the 1.2-dB noise-figure 50-ohm amplifier. The laser-associated noise was much greater than expected from simple shot noise, indicated by the dashed line in Figure 1-2. Well above threshold, the total RF noise was over twice the amplifier noise in the low-noise regions, and here the laser-associated noise component was several times larger than that calculated for shot noise. Frequency spectra of the laser-associated noise were measured and found to be relatively flat over the 1 to 500 MHz band at most laser current settings. In some of the high-noise regions, broad (100-MHz-wide) peaks were observed in the spectra. These results are similar to previously reported RF noise data on Pb-salt diode lasers.⁵

The diffused-junction small-energy-gap HgCdTe photodiodes tend to have weak rectification characteristics, which degrade their wide-bandwidth heterodyne performance. Carrier freezeout occurs at low temperatures in the p-type region, and tunneling in reverse bias gives rise to high junction leakage current. In Figure 1-3 are shown the I-V characteristics of the 190- μ m-dia. HgCdTe photomixer at 20 K in the dark and with an incident laser power of about 50 μ W. The

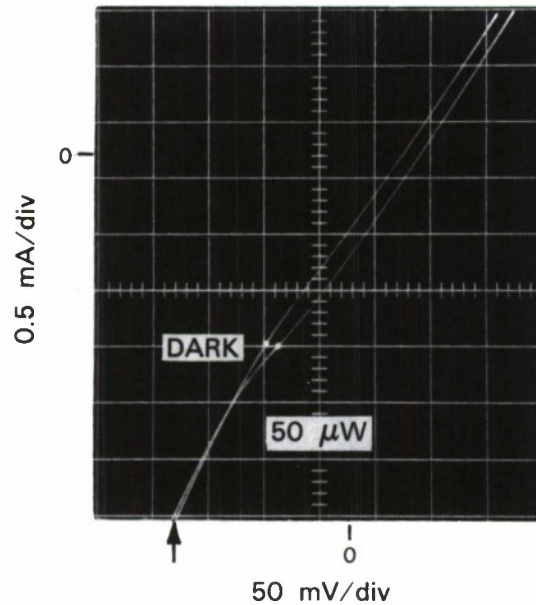


Figure 1-3. Current-voltage characteristics of HgCdTe photodiode mixer in the dark and illuminated with a 50- μ W, 28- μ m local oscillator beam.

series resistance (given by the slope in forward bias) was about 40 ohms, and under illumination the junction shunt resistance was about 40 ohms. Thus only about 10 percent of the RF power available from the LO-induced internal photocurrent (0.6 mA) was delivered to the 50-ohm amplifier, raising the LO power requirement of the photomixer. Here the weak rectification characteristics lead to a photocurrent requirement of about 4 mA.

Blackbody radiometric sensitivity measurements¹ were carried out with the laser biased at about 1.65 A (indicated by the arrow in Figure 1-2), where the ratio of photocurrent to RF noise was maximum. A chopped and synchronously detected 400°C blackbody source was used along with a 19- μ m long-pass filter to block the relatively intense short-wavelength radiation. Only about 13 percent of the available thermal radiation in the 28- μ m region was incident upon the HgCdTe photomixer as a result of losses due to the transmission of the filter (0.30 transmitting), the beam splitter (0.49), and the CsI window (0.94), as well as the reflectivity of the gold mirrors. As shown in Figure 1-4, a S/N of 26 was measured with a 100-MHz IF bandwidth and a 5-s post-detection integration time. Comparing this to the calculated S/N of 1300 for an ideal 28- μ m photodiode heterodyne receiver, we obtain an effective heterodyne quantum efficiency $\eta_{EH} = 2$ percent. This corresponds to an NEP of 3.5×10^{-19} W/Hz at 28 μ m and is the highest sensitivity

reported to date for a wideband 28- μm heterodyne receiver. Similar measurements were made using several frequency bands out to 500 MHz (the range of our low-noise preamplifier), and η_{EH} was found to be relatively independent of frequency.

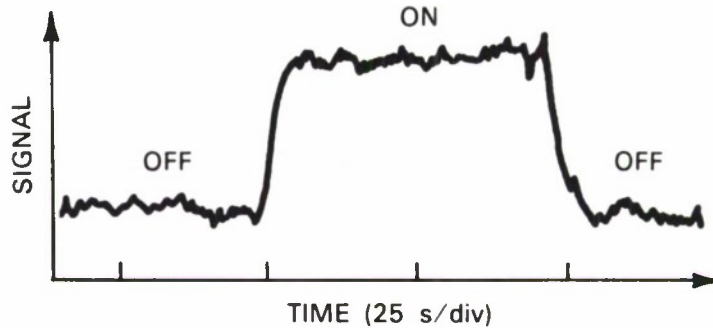


Figure 1-4. Synchronously detected 28- μm heterodyne signal as a function of time with a 400°C blackbody off and on the detector.

Excess laser noise and insufficient LO power for shot-noise-limited operation are responsible for η_{EH} being less than the DC quantum efficiency ($\eta = 40$ percent). Elimination of all excess laser noise would increase η_{EH} by a factor of 2. Then an additional order-of-magnitude improvement could be realized by either increasing the laser power by about an order of magnitude or by improving the photodiode I-V characteristics, or a combination of both. An ideal 28- μm photodiode with $\eta = 100$ percent should be shot-noise-limited at an LO power of 15 μW .

We have recently measured the photocurrent and noise characteristics of narrow-stripe PbSnSe diode lasers² and found that although their power output was less than the broad-area lasers, some devices had negligible excess noise over a significant portion of the current range. We calculate that with a simple substitute of the best of these lasers a 67 percent improvement in performance should be realized, and with an optimum 50/50 beam splitter η_{EH} should further increase to about 5.6 percent. If the long-pass filter were replaced with an efficient grating, the S/N should be increased by an additional factor of over 3 for a single-mode laser, and by a factor of 1.5 for a laser with 50 percent of its power in one mode (which is typical of most of these PbSnSe lasers²). This projected performance makes this long-wavelength infrared heterodyne spectrometer very attractive for remote sensing from a high-altitude platform where atmospheric losses are small. For example, with a 10-MHz resolution bandwidth, the S/N for detecting radiation from the surface of Mars should be over 500/1 in an observation time of less than 30 min., which is comparable to the best 10- μm heterodyne radiometric data.¹

D.L. Spears
R.E. Reeder

1.2 WIDEBAND INTEGRATED-OPTICS ELECTROOPTIC INTENSITY MODULATOR FOR 3.39- μm OPERATION

Waveguides that are single mode at $\lambda = 3.39 \mu\text{m}$ have been fabricated in LiNbO_3 by indiffusion of Ti. Mach-Zehnder interferometers using these waveguides have been used to electrooptically modulate the intensity of the radiation at this wavelength. One modulator design has achieved a linear small-signal 3-dB bandwidth of 1.8 GHz. An extinction ratio of 18.9 dB was obtained for a TE-polarized guided mode with an applied voltage, $V_\pi = 31 \text{ V}$. This value of V_π is consistent with predictions based upon modulator results at $0.85 \mu\text{m}$ and λ^2 scaling rules, which apply if there is no dispersion in the electrooptic coefficients.

High-performance wideband, guided-wave modulators have been developed for $\lambda < 1.6 \mu\text{m}$ (References 6 and 7). These are the first such devices designed for use in the 3- to 4- μm region where proposed long-distance, repeaterless optical-fiber data links are to operate based upon the projected low loss ($\approx 10^{-3} \text{ dB/km}$) of heavy-metal fluoride glasses.⁸ A high data-transmission rate will be required in these long-distance links, and it is questionable whether the cryogenically cooled lead-salt laser (the semiconductor laser of current choice for $\lambda > 3 \mu\text{m}$) can be efficiently modulated at the required rates, as present lasers have exhibited slow ($\approx 1.5 \text{ ns}$) turn-on transients.⁴ Thus, external modulators as described here may be essential for $\lambda > 3 \mu\text{m}$, where there exists currently a very large effort in fiber development.⁹

A schematic diagram of the guided-wave Mach-Zehnder interferometric modulator in which the waveguide sections are single mode is shown in Figure 1-5. Before fabricating this modulator, Ti-indiffused waveguides of different designs were fabricated on LiNbO_3 and evaluated at $3.39 \mu\text{m}$.

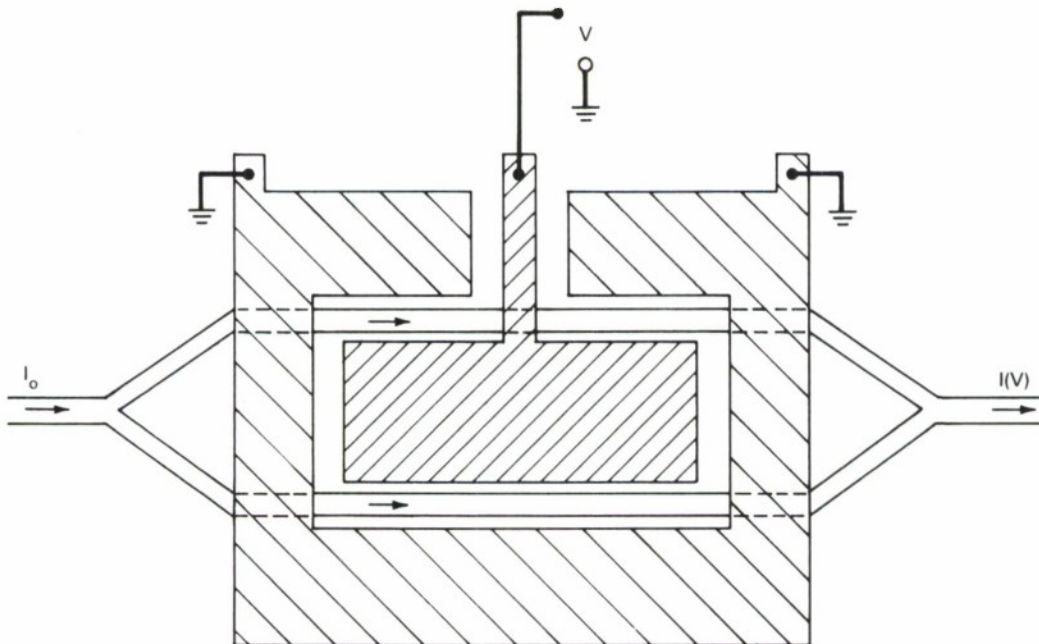


Figure 1-5. Schematic of guided-wave Mach-Zehnder interferometric modulator with center-topped electrode. The two Y junctions have 2° full branching angles, and the direction of optical propagation (except at these bends) is in the y -direction. The $1\text{-}\mu\text{m}$ -thick Cr/Au electrodes are 0.8 cm long and are fabricated on a $2000\text{-}\text{\AA}$ -thick SiO_2 buffer layer. The interferometer arms are 1.8 cm long and are separated by $100 \mu\text{m}$.

In one design, fabrication conditions were chosen so as to maintain the same maximum guide index as waveguides developed for $\lambda = 0.85 \mu\text{m}$ (Reference 6) while scaling the waveguide width and depth approximately as λ . Near- and far-field mode patterns at $3.39 \mu\text{m}$ indicated single-mode propagation for $18\text{-}\mu\text{m}$ -wide waveguides made in this manner. In a second design the dielectric discontinuity was increased by increasing the Ti doping, while the waveguide width was decreased to preserve the single-mode character.

The performance of a modulator made with waveguides of the first design was summarized in the first paragraph above. Figure 1-6 is a photograph of the electrical input and detected optical output of this modulator for TE-polarized $3.39\text{-}\mu\text{m}$ input radiation when DC-biased to its half intensity point with 15.5 V . Note that over two complete π phase flips are produced by the 70-V sinusoidal input. The product of the measured V_π and the modulator electrode length (8 mm) equaled $248 \text{ V}\cdot\text{mm}$ and $960 \text{ V}\cdot\text{mm}$ for TE and TM polarization, respectively; this is in excellent agreement with predictions from $\lambda = 0.85\text{-}\mu\text{m}$ modulator data.⁶

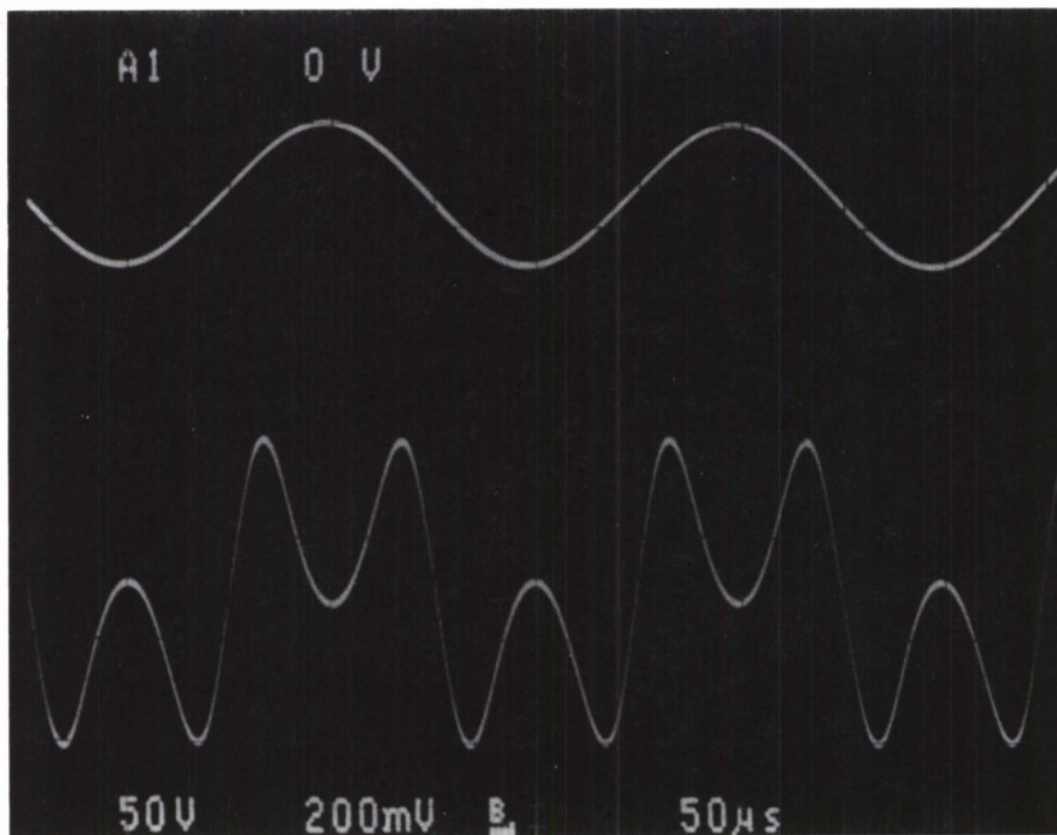


Figure 1-6. Top trace is 70-V peak-to-peak sinusoid used as the modulator drive signal. Bottom trace is modulator output. Modulator was DC-biased to its half intensity point with 15.5 V ($V_\pi/2$). Two π phase flips are seen.

The modulator was terminated in $50\ \Omega$ and its small-signal linear frequency response measured. Figure 1-7 compares the experimental data at $3.39\ \mu\text{m}$ with the theoretical model of the RLC circuit, shown in the inset, with the parameters either measured or calculated. The agreement is very good.

R.H. Rediker
R.A. Becker
T.A. Lind

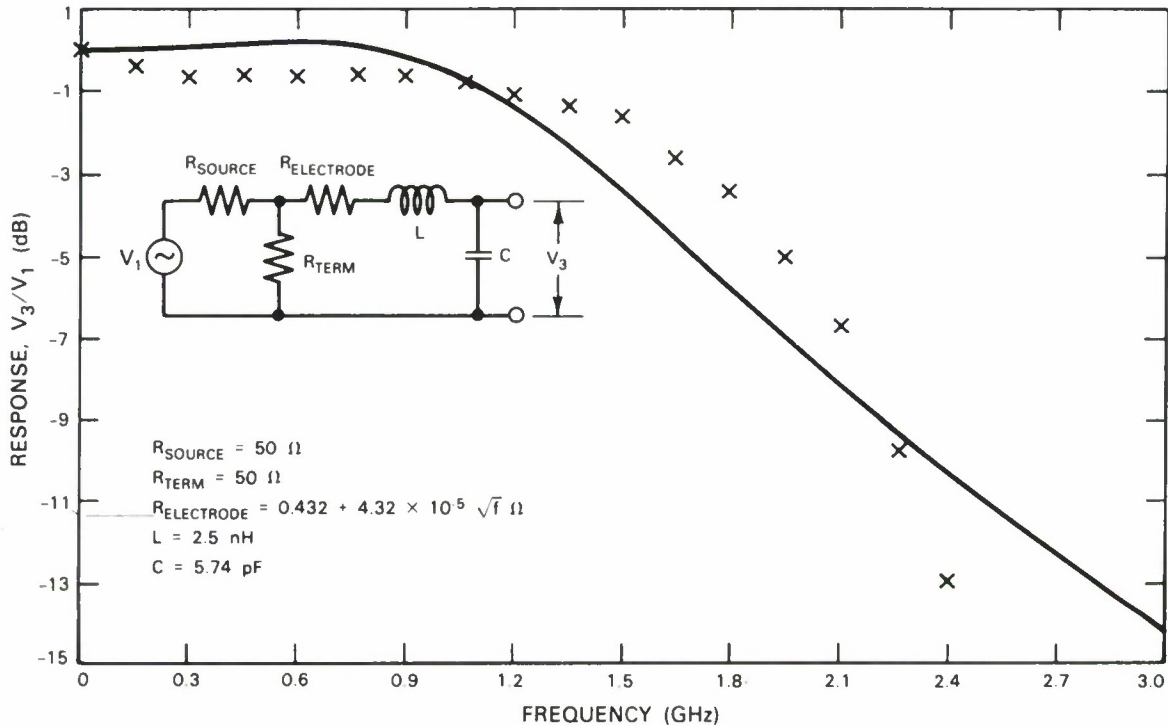


Figure 1-7. Linear small-signal frequency response of modulator. x's are measured response. Solid line is predicted by RLC equivalent circuit.

1.3 InP p-COLUMN JFET

Fully ion-implanted, depletion-mode JFETs have recently been fabricated on semi-insulating InP substrates. These FETs utilize a periodic array of p^+ columns¹⁰ implanted through an n-type channel region, as illustrated in Figure 1-8. In this device the channel region is laterally pinched off from two sides, eliminating channel-substrate interface effects. p-column structures also offer the possibility of fabricating both depletion mode and enhancement mode devices on the same wafer by simply adjusting the spacing of the p columns on the implantation mask. The operation mode of a conventional JFET is determined by either the p^+ layer depth or the channel doping, either of which requires a separate implant step.

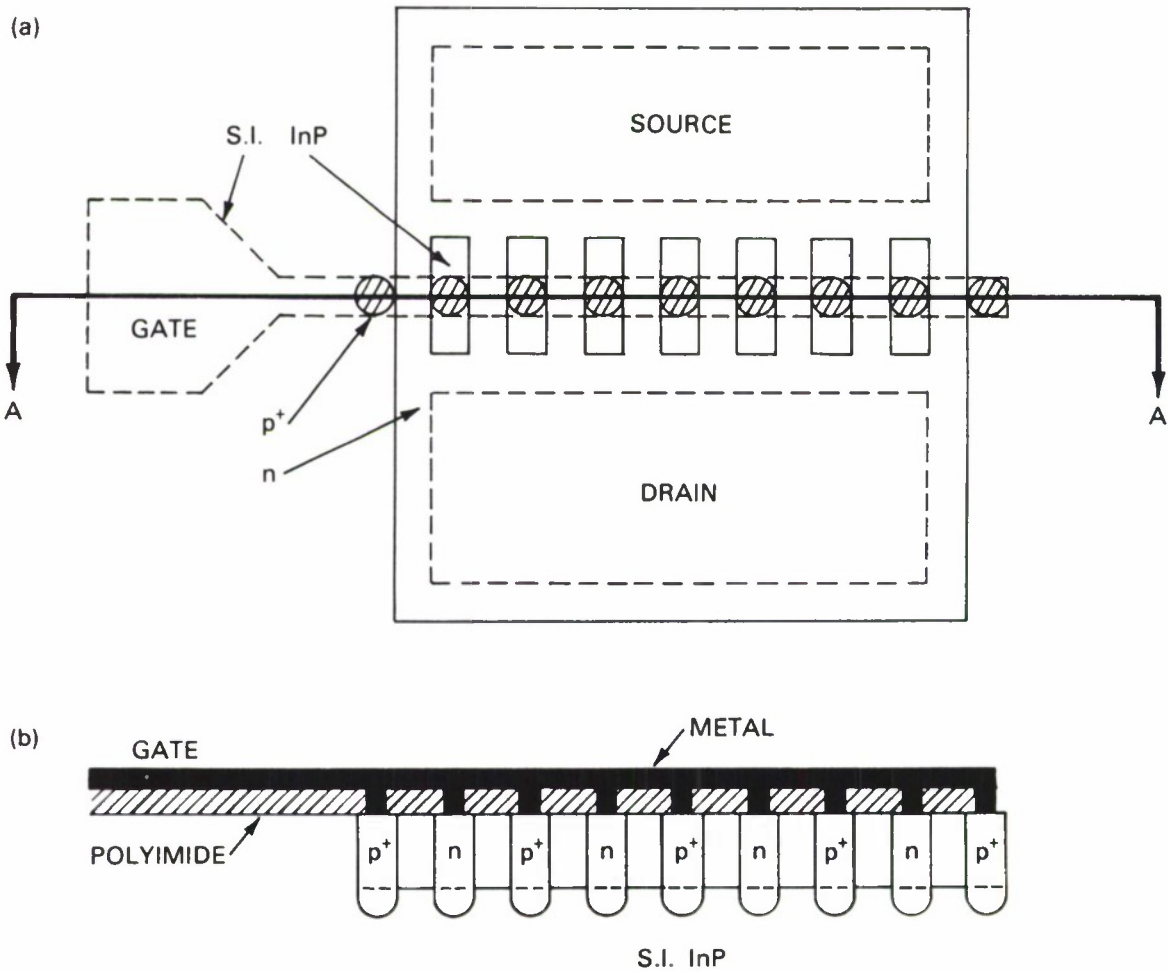


Figure 1-8. p-column JFET (a) top view; (b) gate cross section A-A.

The n-type channel region of the JFETs was formed by implanting Si^+ ions into an Fe-doped, 100-oriented InP substrate. A comb-like channel structure, as shown in Figure 1-8(a), was employed in order to reduce parasitic capacitance. Columns of $4\text{-}\mu\text{m}$ -diameter spaced $2\text{ }\mu\text{m}$ apart were then implanted with Be^+ ions to form the p^+ gate regions. The Be^+ implant schedule (implant energies and dosages) was chosen to produce a uniform p^+ region deeper than the n-type channel. Following implantation, the sample was annealed at 750°C for 5 min. using a PSG encapsulation. Microalloyed Ni/Ge/Au was used to contact the source-drain regions, while Zn/Au was used for the p^+ column regions. The sample surface was then passivated using polyimide, and the gate-pad and final source-drain metallization was applied using a lift-off technique.

Test diodes fabricated along with the FETs exhibited forward current turn-on voltages of 0.7 V and reverse breakdown voltages of 15 V. The transconductance of a typical device, as shown in Figure 1-9, is about 1 mS, which translates to about 60 mS/mm gate width. RF measurements performed on selected packaged devices indicate a unity-power-gain frequency (f_{max}) of 7 GHz. The f_{max} attained for these 4- μm InP p-column devices indicate that InP devices of this type should have better performance characteristics than similar devices fabricated in GaAs (Reference 10). The development of a self-aligned 1- μm p-column process and reduction of parasitics should result in devices with substantially improved high-frequency performance ($f_{max} > 25$ GHz).

J.D. Woodhouse
J.P. Donnelly
W.J. Piacentini

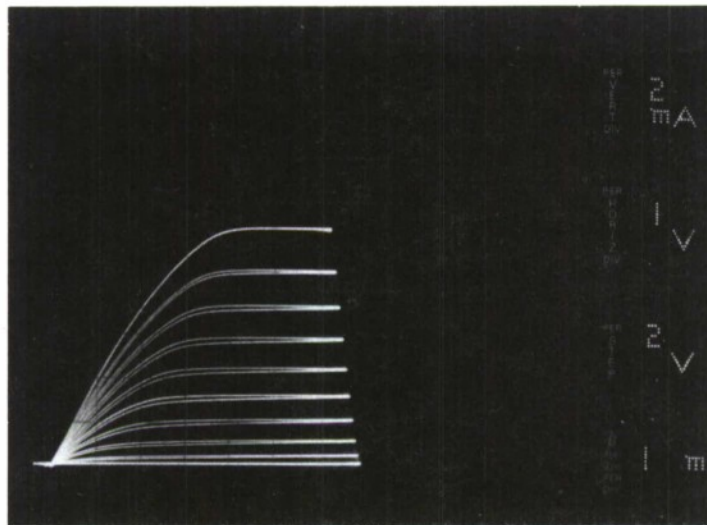


Figure 1-9. Characteristic curves for a 4- μm p-column JFET.

REFERENCES

1. T. Kostiuk and M.J. Mumma, *Appl. Opt.* **22**, 2644 (1983).
2. K.J. Linden, *Proc. SPIE* **438**, 2 (1983).
3. Solid State Research Report, Lincoln Laboratory, M.I.T. (1981:4), p.12, DTIC AD-A114189/4.
4. D.L. Spears, Digest of 8th Intl. Conf. on IR and MM Waves, Miami Beach, Florida, 12-17 December 1983, paper T2.8.
5. R.T. Ku and D.L. Spears, *Opt. Lett.* **1**, 84 (1977).
6. R.A. Becker, *IEEE J. Quantum Electron.* **20**, 723 (1984).
7. R.C. Alferness, *IEEE Trans. Microwave Theory Tech.* **30**, 1121 (1982).
8. D.C. Tran, G.H. Sigel, Jr., K.H. Levin, and R.J. Ginther, *Electron Lett.* **18**, 1046 (1982).
9. See, for example, G.H. Sigel, Jr., Ed., Special Issue of Low Loss Fibers, *J. Lightwave Tech.* **2**, 565 (1984).
10. A. Kazuyoshi *et al.*, *IEEE Electron Device Lett.* **EDL-1**, 83 (1980).

2. QUANTUM ELECTRONICS

2.1 TRANSIENT CARRIER DENSITY AND LIGHT OUTPUT MEASUREMENTS OF PULSED DIODE LASERS

Short light pulses from diode lasers can be generated by high-frequency modulation of the injection current. While the light output* and gain† of diode lasers have been measured under such transient conditions, they have never been measured together so as to give a more complete picture of diode laser dynamics. We report here measurements of both the carrier density and light output of pulsed GaAlAs diode lasers.

The measurements were made by sampling both the diode transmission and light output with the 5-ps light pulses from a mode-locked dye laser. The diodes were driven with 90-ps current pulses from a comb generator in addition to a DC bias current. The dye laser was tuned to the diode laser wavelength and had sufficient intensity to bleach the diode gain medium, so that the difference between the carrier density at any particular instant and that at transparency was determined. Multipass effects in the diode cavity were neglected because of the gain depletion and the short cavity lifetime compared with the gain lifetime and current pulse duration. The dye laser probe was polarized orthogonally to the diode laser radiation so the two lasers could be optically isolated with a polarizer and to keep the normal diode laser output from reaching the detector. The light output measurement was made by the sum-frequency sampling method used by Duguay and Damen in a related application.*

The experiments were performed using a beat-frequency sampling technique that eliminated the translated mirrors which form the variable optical delay line used in most picosecond pulse sampling experiments. The diode laser was pulsed at 492.280049 MHz and the dye laser probed at a 246.140000-MHz repetition rate. Thus the dye laser pulses sampled through the 2.03-ns interval between diode laser pulses every 20.3 ns. This scheme allowed real-time display of the measurements on an oscilloscope, made long time scans possible, and eliminated the optical alignment problems entailed in a long optomechanical delay line.

Four measurements are shown in Figure 2-1. The experimental conditions were identical in each case, except for the DC injection currents. Case (d) shows the below-threshold behavior, where no diode laser light is emitted and the carriers recombine at the gain-medium lifetime rate after buildup from the current pulse. Strong gain depletion as diode laser light is emitted is observed in all the above-threshold cases. The multiple pulsing observed in case (a) is due to relaxation oscillation behavior triggered by the current pulse. A carrier density buildup time longer than the current pulse delivered to the laser mount is seen in the data. The combined electrical characteristics of the diode and its mount may cause this broadening even though the mount was designed to match the transmission line impedance and to have small parasitic effects.

* M.A. Duguay and T.C. Damen, *Appl. Phys. Lett.* **40**, 667 (1982).

† W.Lenth, *Opt. Lett.* **9**, 396 (1984).

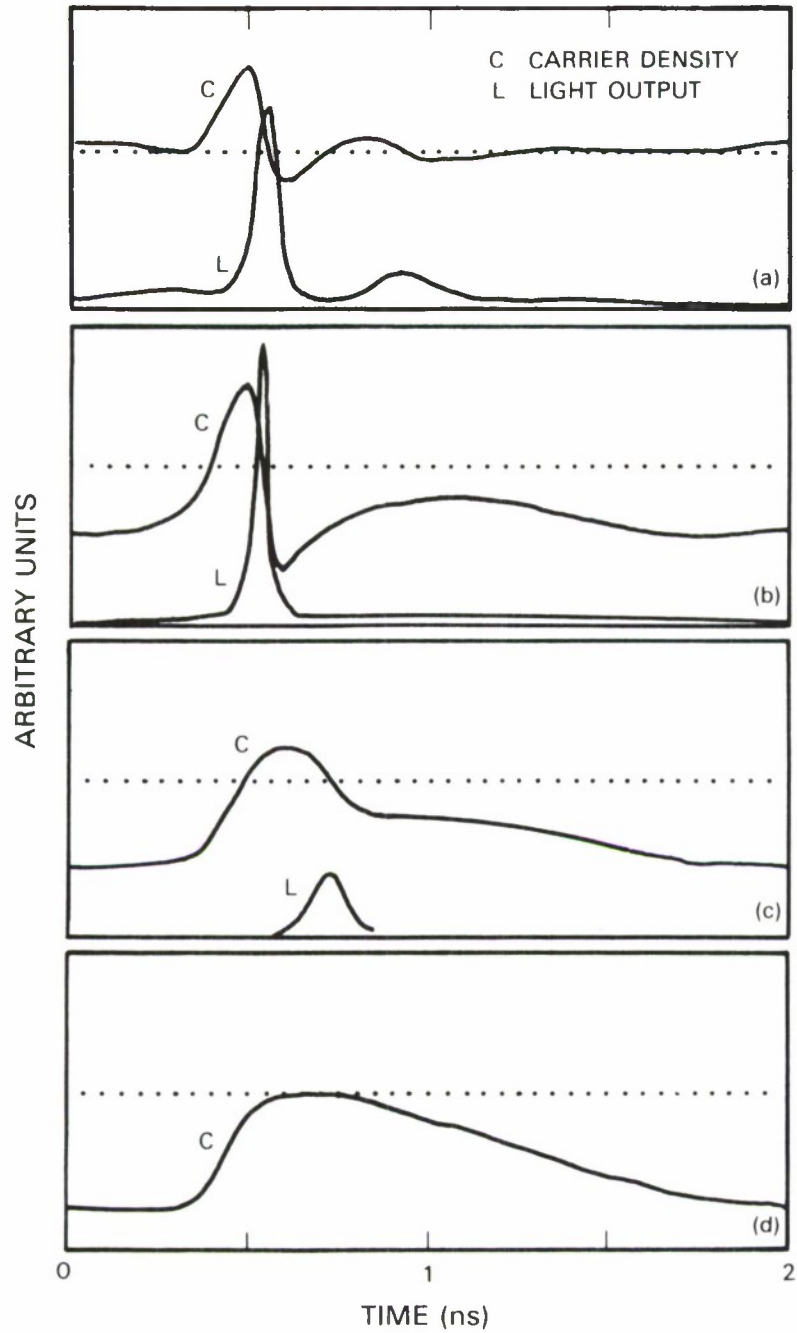


Figure 2-1. Measured carrier density C and light output L as a function of time for DC bias currents of (a) 79 mA, (b) 72 mA, (c) 66 mA, and (d) 61 mA. Dotted line in each box represents estimated carrier density at threshold. There is no light output curve for case (d) since the diode was below threshold.

Although additional carrier injection due to strong current-pulse broadening may have caused the fast gain recovery in case (b), it is likely that lateral carrier diffusion is responsible. Diffusion has an important damping effect in the channeled substrate planar (CSP) lasers used in these experiments.* Modeling of the gain, light, and carrier diffusion dynamics will provide insight into this question.

B. C. Johnson
A. Mooradian

* N. Chinone, K. Aiki, M. Nakamura, and R. Ito, IEEE J. Quantum Electron. **QE-14**, 625 (1978).



3. MATERIALS RESEARCH

3.1 ZONE-MELTING RECRYSTALLIZATION OF Si- AND Ge-ON-INSULATOR FILMS

In the program on preparing Si-on-insulator (SOI) films by zone-melting recrystallization (ZMR) using graphite strip heaters,¹ major advances in our effort to eliminate sub-grain boundaries (subboundaries) from the films have been achieved by improving the overall thermal stability and uniformity of the graphite-strip-heater system. Figure 3-1 shows Nomarski micrographs of two recrystallized SOI films that have been defect etched to reveal the subboundaries. Figure 3-1(a), which was obtained for an SOI wafer in which the Si film and underlying SiO₂ layer are each $\sim 0.5 \mu\text{m}$ thick, shows branched subboundaries. A dramatically different morphology is shown in Figure 3-1(b), which was obtained for a wafer in which the Si film and underlying SiO₂ layer are $\sim 1 \mu\text{m}$ thick. Here the subboundaries are straight and unbranched, as a result of the extreme thermal stability of the liquid-solid interface during recrystallization. These subboundaries are also more widely spaced, indicating that the thermal gradient was lower.² Until recently such unbranched subboundaries were rarely observed in films less than $5 \mu\text{m}$ thick. Now, however, we routinely obtain this morphology over most of the area of films as thin as $1 \mu\text{m}$ and have even observed it in some $0.5\text{-}\mu\text{m}$ films. Recent results on the dependence of subboundary morphology on the thickness of the Si film and the SiO₂ layer are summarized in Figure 3-2.

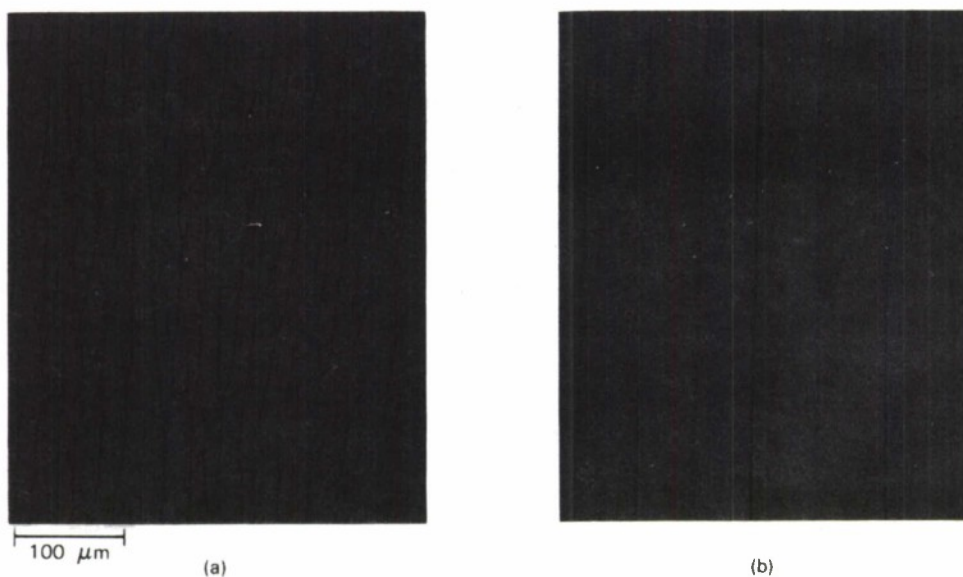


Figure 3-1. Optical micrographs of (a) branched and (b) unbranched subboundaries in recrystallized SOI films.

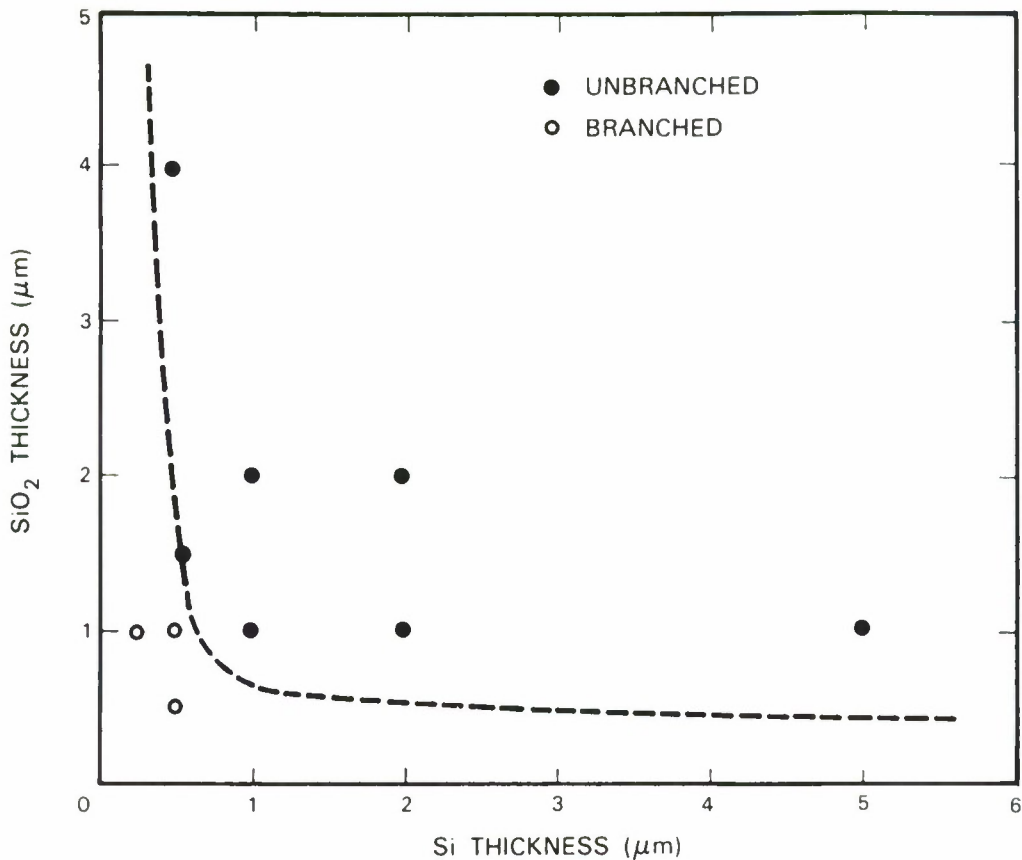


Figure 3-2. Regions of branched and unbranched subboundaries as a function of Si and SiO₂ thickness.

An even more significant development is illustrated by Figure 3-3, which is a Nomarski micrograph of a recrystallized film 2 μm thick that was defect etched. The subboundaries have been replaced by less extended defects, shown by transmission electron microscopy to be either dislocation clusters arranged in linear arrays or individual dislocations forming diffuse bands, and the remaining area is nearly defect-free. Furthermore, the individual dislocations can be removed by annealing, although the clusters appear to be thermally stable. So far we have observed these new defects only in limited areas of 2-μm films, but we are now hopeful that further improvements in the strip-heater technique will make it possible to entirely eliminate the subboundaries even from 0.5-μm films.

Stringent flatness requirements are imposed on SOI wafers by the photolithographic process used in VLSI fabrication. A significant reduction in warp has been achieved over the past year by means of a number of changes in ZMR technique. These include the improvement in the thermal uniformity of the graphite-strip-heater system, a reduction in the heating and cooling rates before and after ZMR to ~4°C/s, the use of 0.020-in.-thick Si substrates to provide increased

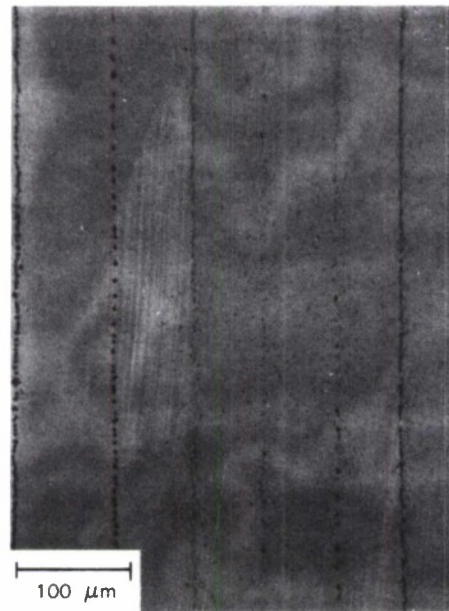


Figure 3-3. Optical micrograph of a recrystallized film showing unbranched subboundaries and other less extended defects.

mechanical strength, and an increase in the scan speed. The ZMR wafers can now meet the requirements for fabricating circuits with $\sim 2\text{-}\mu\text{m}$ geometries. Figure 3-4 shows interference patterns obtained with a high-angle-of-incidence laser flatness monitor for a bare Si wafer (on the left) and an SOI wafer after recrystallization (on the right). These patterns, which were measured with the wafers mounted on a vacuum chuck, provide a topographic map of the wafer surface in which each interference fringe corresponds to a height of $\sim 4\ \mu\text{m}$. The recrystallized wafer, like the bare Si wafer, is found to have a total warp of $< 4\ \mu\text{m}$, peak to valley.

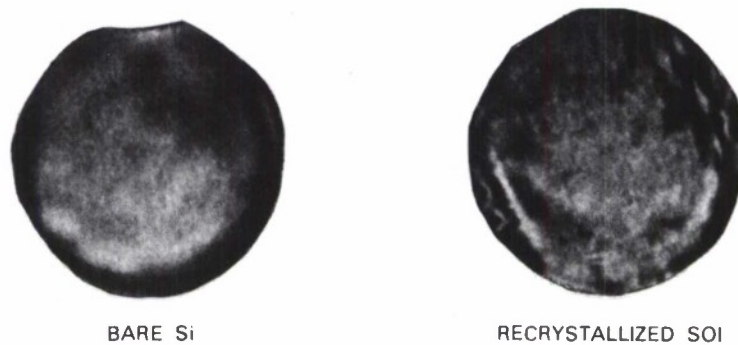


Figure 3-4. Interference patterns with a $4\text{-}\mu\text{m}/\text{fringe}$ sensitivity for 3-in. (a) bare Si wafer and (b) recrystallized SOI wafer.

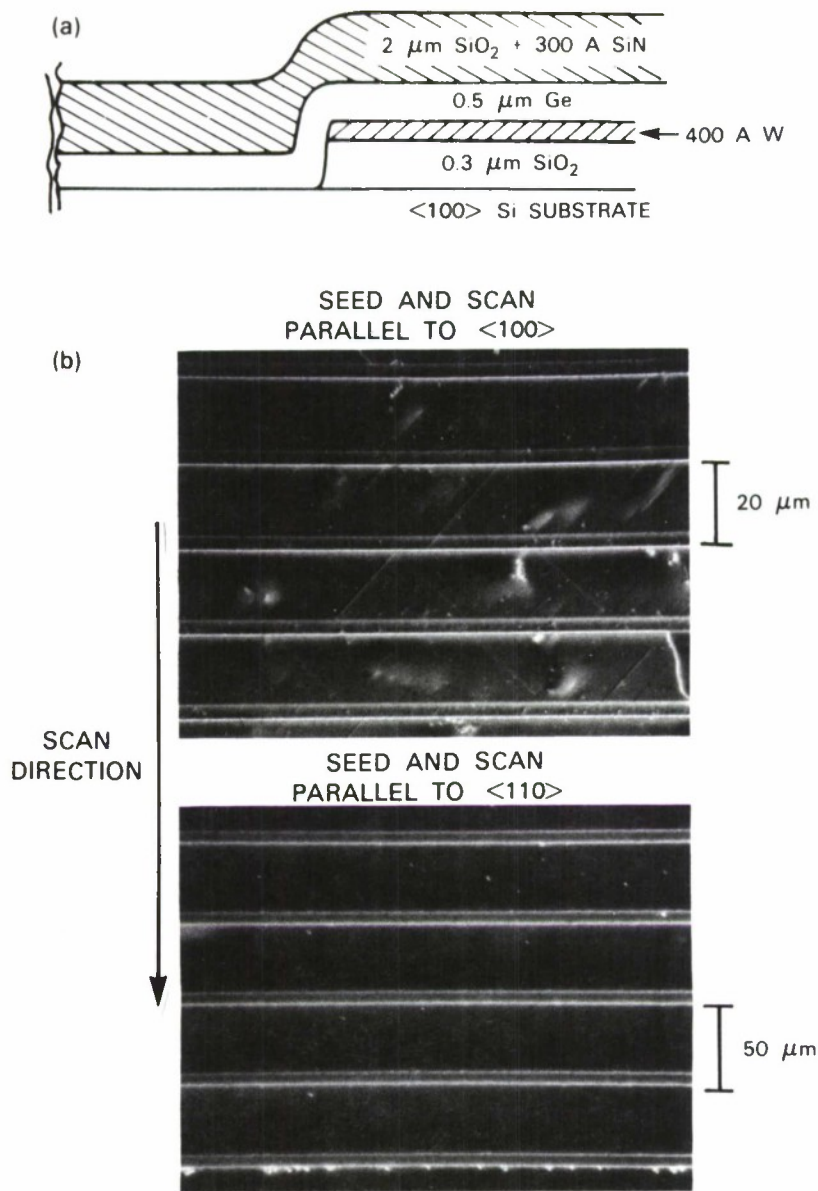


Figure 3-5. (a) Seeded Ge-on-insulator sample structure and (b) optical micrographs of Ge-on-insulator wafers after ZMR with seed and scan parallel to $\langle 100 \rangle$ and $\langle 110 \rangle$ directions.

146621-N-01

As a further step in utilizing the graphite-strip-heater ZMR technique, we have recently initiated an effort to use this technique for growing high-quality single-crystal Ge films on SiO₂-coated Si wafers.³ By providing substrates for epitaxial growth of GaAs, the growth of such films could make a major contribution to monolithic GaAs/Si device integration. Figure 3-5(a) shows the sample structure that has yielded the best overall surface morphology to date. A thin W film is deposited by e-beam evaporation on an SiO₂-coated $\langle 100 \rangle$ Si substrate. Stripe openings for seeding are then lithographically defined and formed by selectively etching away the W and SiO₂ to expose the Si substrate. A polycrystalline layer of Ge is deposited by e-beam evaporation, followed by capping layers of sputtered SiO₂ and Si₃N₄. The W buffer layer and the capping layers are necessary to insure wetting by the Ge film and to obtain smooth surface morphology.

The effect of seed and scan orientation on the surface morphology of the ZMR Ge films is shown in Figure 3-5(b) by Nomarski micrographs of two recrystallized samples that were defect etched. The upper sample, with seed and scan direction parallel to $\langle 100 \rangle$ directions of the Si substrate, contains many microtwins, which are symptomatic of a growth front with $\{111\}$ facets, as has been observed for Si. This sample does not contain a tungsten buffer layer and hence was more susceptible to cap failure and agglomeration of the Ge film. The lower sample, with seed and scan direction parallel to $\langle 110 \rangle$ and with a tungsten buffer layer, shows a very smooth surface morphology with very few defects. Our best results to date have been achieved for 50- μ m-square Ge/W/SiO₂ islands with edges parallel to $\langle 110 \rangle$ directions. Figure 3-6 shows low- and high-magnification Nomarski micrographs of such a sample after ZMR and defect etching. A thickness variation of ~ 200 Å was observed within the islands. The surface showed a slight texturing, and careful inspection revealed a few low-angle grain boundaries. The individual grains are

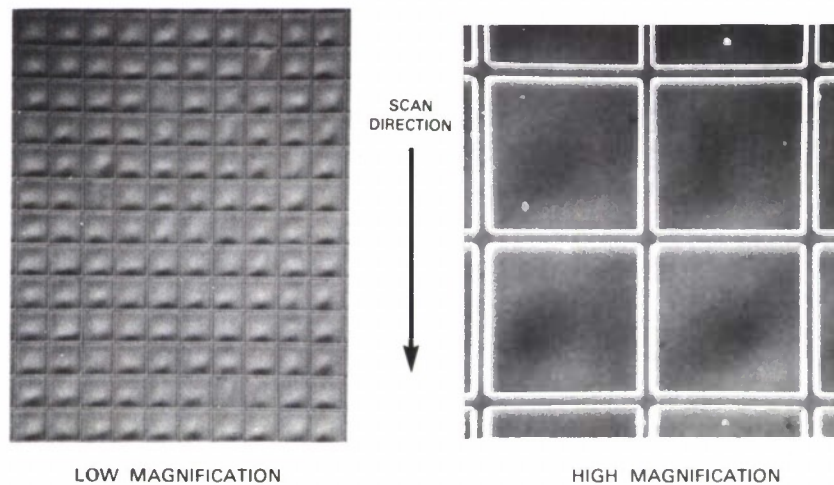


Figure 3-6. Nomarski micrographs of seeded 50- μ m Ge-on-insulator islands after ZMR and defect etching.

more clearly delineated by scanning electron microscopy, as shown in Figure 3-7. We have verified by x-ray and electron diffraction that the Ge films have the $\langle 100 \rangle$ orientation of the substrate, and no W is detected in the Ge films by Auger analysis, which has a detection limit of ~ 1 percent.

C.K. Chen	B-Y. Tsaur
M.W. Geis	J.C.C. Fan
H.K. Choi	

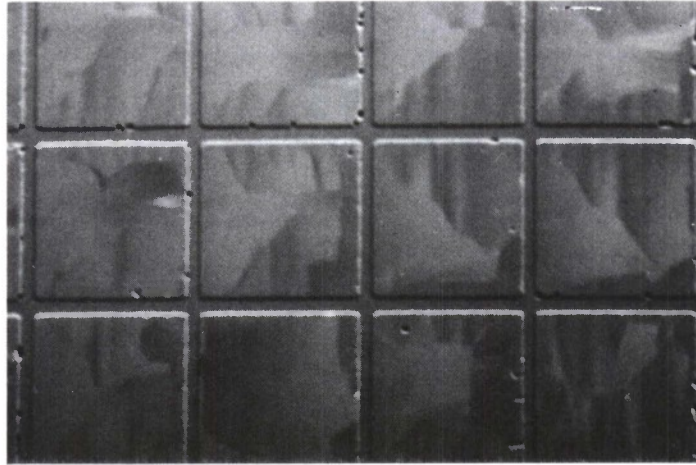


Figure 3-7. Scanning electron micrograph of seeded 50- μm Ge-on-insulator islands after ZMR.

3.2 MOSFETs FABRICATED USING SELF-ALIGNED SILICIDE TECHNOLOGY

In an earlier report⁴ we described a technique that employs ion-beam mixing followed by rapid thermal annealing for the selective formation of smooth tungsten silicide (WSi_2) films on patterned SiO_2 -coated Si substrates and the simultaneous formation of shallow p-n junctions. We have now used this technique to fabricate n- and p-channel MOSFETs with self-aligned WSi_2 gate, source, and drain. The good electrical characteristics of these devices indicate that the new technique should be useful in the fabrication of CMOS integrated circuits.

The process sequence for MOSFET fabrication is shown schematically in Figure 3-8. The active device area was defined by etching an opening in a 0.5- μm -thick field oxide formed by thermal oxidation of the Si substrate. A gate oxide about 30 nm thick was formed by reoxidation of the exposed substrate, and a 0.5- μm -thick polycrystalline Si film was then deposited. Plasma etching in a parallel-plate reactor was used to define a poly-Si gate with vertical sidewalls, as shown in Figure 3-8(a). The gate oxide was removed from the source and drain regions by chemical etching, slightly undercutting the gate, and a film of W metal about 30 nm thick was deposited over the entire wafer by electron-beam evaporation normal to the surface. Because of the vertical profile of the gate, very little W was deposited on the sidewalls. The wafer was

implanted with As^+ and BF_2^+ ions for n- and p-channel devices, respectively [Figure 3-8(b)]. (BF_2^+ ions were used, rather than the B^+ ions conventionally implanted to form p^+ layers, because their greater mass results in more effective ion-beam mixing.) The ion energies were chosen to locate the peak implanted concentrations near the W-Si interface, and the ion doses were 2 to $5 \times 10^{15} \text{ cm}^{-2}$, typical values for MOSFET source and drain implants.

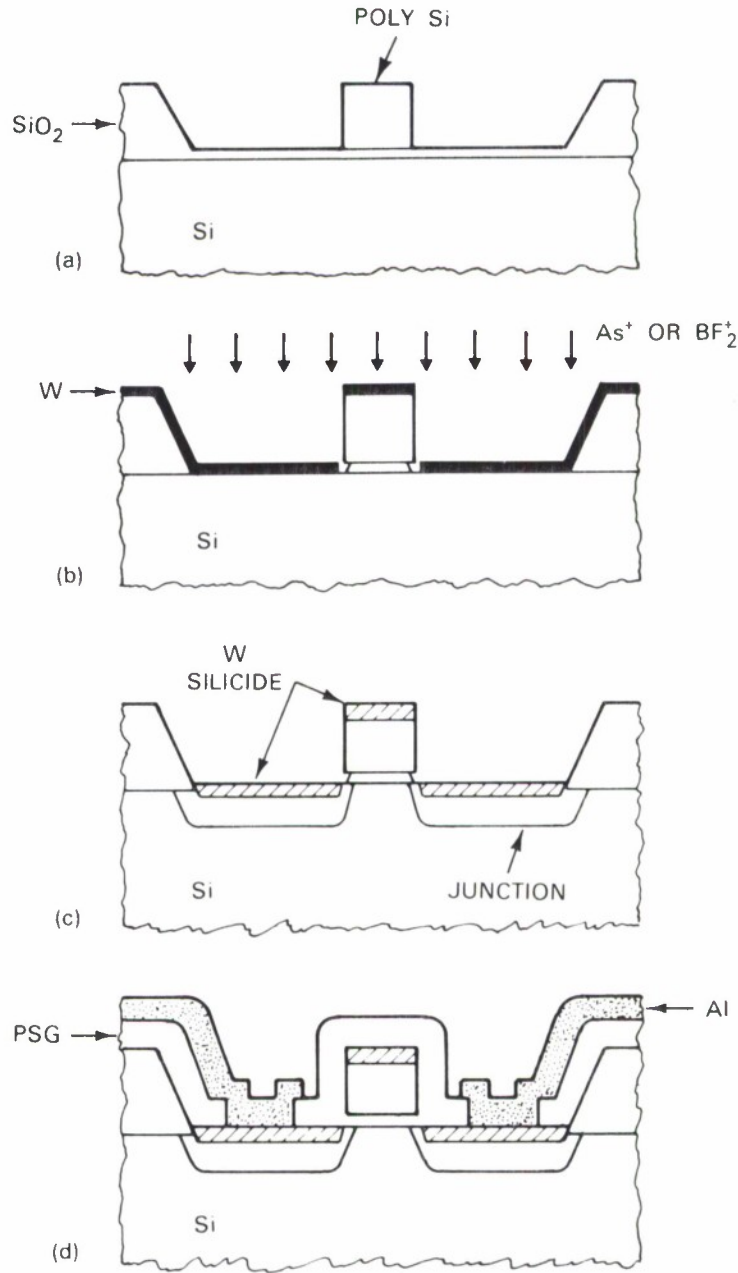


Figure 3-8. Process sequence for MOSFETs fabricated using self-aligned silicide technology.

Rapid thermal annealing was performed in two steps, in each of which the maximum temperature was maintained for about 10 s. After the first anneal, for which the maximum temperature was 850°C, selective chemical etching was used to remove unreacted W, producing the structure shown in Figure 3-8(c). Figure 3-9, which is a scanning electron micrograph of the surface after etching, shows that self-aligned WSi₂ has been formed on the source, gate, and drain, and that there is no residual W on the field oxide or gate sidewalls. The second annealing step, for which

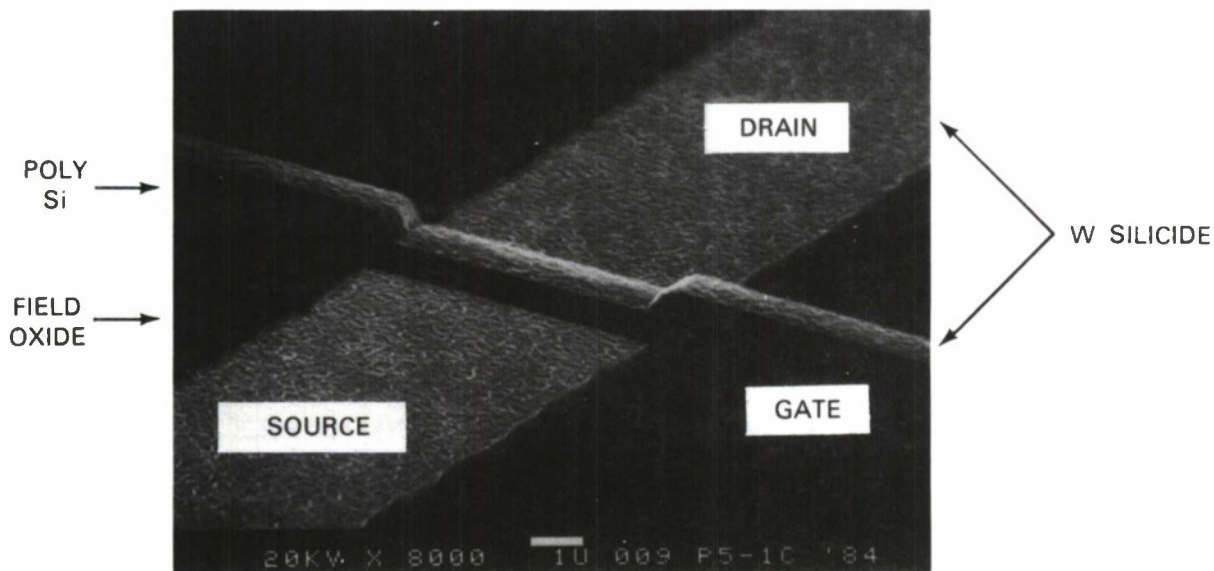


Figure 3-9. Scanning electron micrograph of MOSFET surface after removal of W by selective etching.

the maximum temperature was ~1000°C, reduced the sheet resistance of the WSi₂ and achieved nearly complete electrical activation of the implanted dopants. The devices were completed by deposition of a passivating layer of phosphosilicate glass and finally Al metallization [Figure 3-8(d)].

Figure 3-10 shows the gate-source (gate-drain) characteristics of an n-channel MOSFET with a gate length of 1.5 μm and gate width of 48 μm. The breakdown voltage, which exceeds 20 V, is comparable to that of conventional poly-Si gate devices. Similar characteristics were obtained for the p-channel devices. Typical transistor characteristics for n- and p-channel MOSFETs are shown in Figures 3-11(a) and (b), respectively. Both types of devices have well-behaved characteristics, with drain-source breakdown voltages of 12 and 15 V, respectively. For both types the measured subthreshold leakage currents were <1 pA, indicating that the source and drain p-n junctions were of good quality.

150176-R

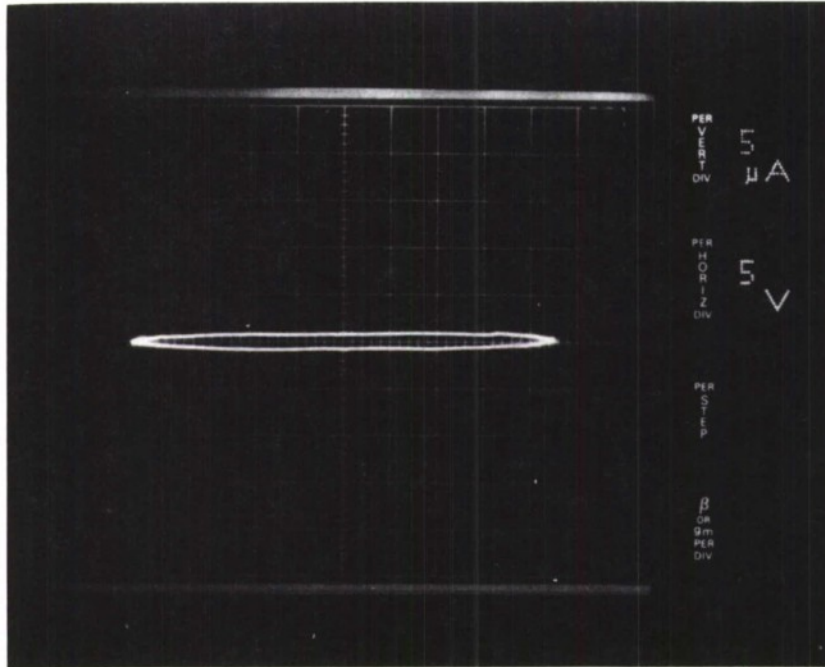
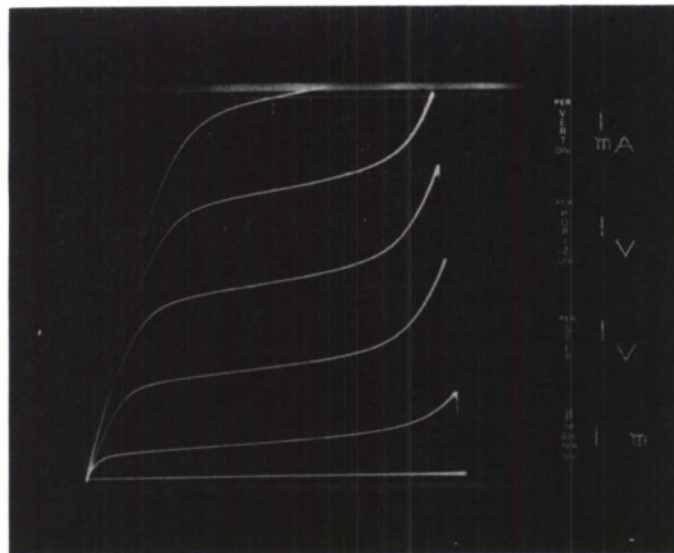


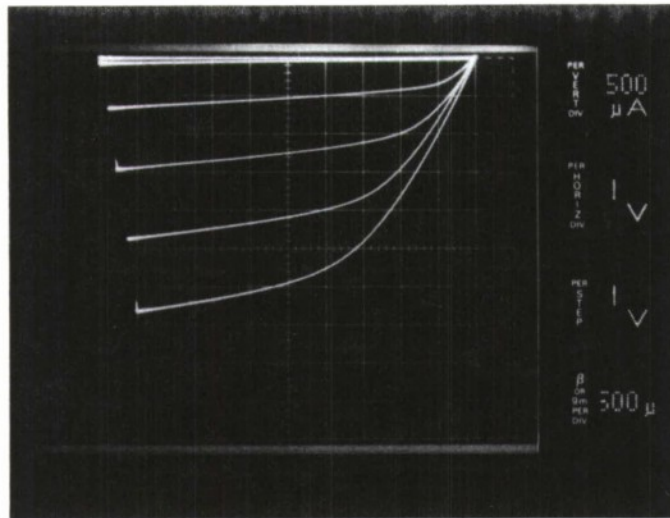
Figura 3-10. Gata-sourca (gate-drain) characteristic of n-channel MOSFET.

150177-R



(a)

Figura 3-11. Transistor characteristics of (a) n-channel and (b) p-channel MOSFETs.



(b)

Figure 3-11. Continued.

150178-R

For self-aligned silicide technology, WSi_2 offers several advantages over the silicides of Ti (Reference 5) and Pt (Reference 6). Since WSi_2 exhibits good thermal stability in contact with Si, high-temperature processing can be performed without degradation of the gate oxide and p-n junctions. The reaction of W with SiO_2 is thermodynamically unfavorable, so that WSi_2 is a good candidate for self-aligned processing. In addition, WSi_2 can be conveniently oxidized to produce a passivating SiO_2 layer.⁷ Finally, WSi_2 forms a good diffusion barrier against Al-Si interaction and can therefore be used for shallow-junction devices.

B-Y. Tsauro
C.H. Anderson, Jr.

3.3 GaAs OPTICAL MESFET DETECTORS FABRICATED ON A MONOLITHIC GaAs/Si SUBSTRATE

The fabrication of GaAs and Si devices on the same chip is an important step in the evolution of microelectronics toward the integration of optical and electronic functions. Although GaAs solar cells,⁸ LEDs,⁹ double-heterostructure diode lasers,¹⁰ MESFETs,¹¹⁻¹³ and MODFETs¹⁴ have been fabricated on monolithic GaAs/Si (MGS) wafers, there has been no report of high-speed optical detectors on MGS wafers. We now report the fabrication of such MGS optical detectors—specifically, GaAs optical MESFETs (OPFETs)—in a GaAs layer grown by molecular beam epitaxy directly on a Si substrate.

Several workers¹⁵⁻¹⁷ have fabricated GaAs OPFETs on conventional GaAs wafers. These devices have shown picosecond response times and reasonable gain. For MGS applications OPFETs may offer advantages over other types of optical detectors, such as avalanche photodiodes. Since OPFETs require no junctions or high-field regions, they are less sensitive to material

quality, which may not reach the same level for MGS GaAs layers as for conventional GaAs materials. Further, since they require no additional epitaxial growth or processing steps beyond those necessary for MESFET logic devices, OPFETs can easily be incorporated into integrated circuits.¹⁸

The MGS OPFETs were fabricated with the same configuration and on the same wafer that we previously used for conventional MGS MESFETs.¹³ Our best results to date have been obtained from a device with a gate length of $2\mu\text{m}$, a gate width of $200\mu\text{m}$, and a DC transconductance of 72mS/mm . This device was packaged in a simple two-terminal stripline package, which did not permit substrate biasing. The circuit used to bias the packaged OPFET is shown in Figure 3-12.

Pulsed laser illumination at 840nm was obtained by applying current pulses to a commercial CW GaAlAs double-heterostructure laser diode. The specified rise time of the radiant flux from the laser, which determines the shortest detector response time that can be measured, is 100 to 800ps . The last diode was directly coupled to an optical fiber to permit rapid positioning of the illumination over the channel of the OPFET. The peak power from the fiber was 2mW , but the output divergence made absolute responsivity measurements impossible.

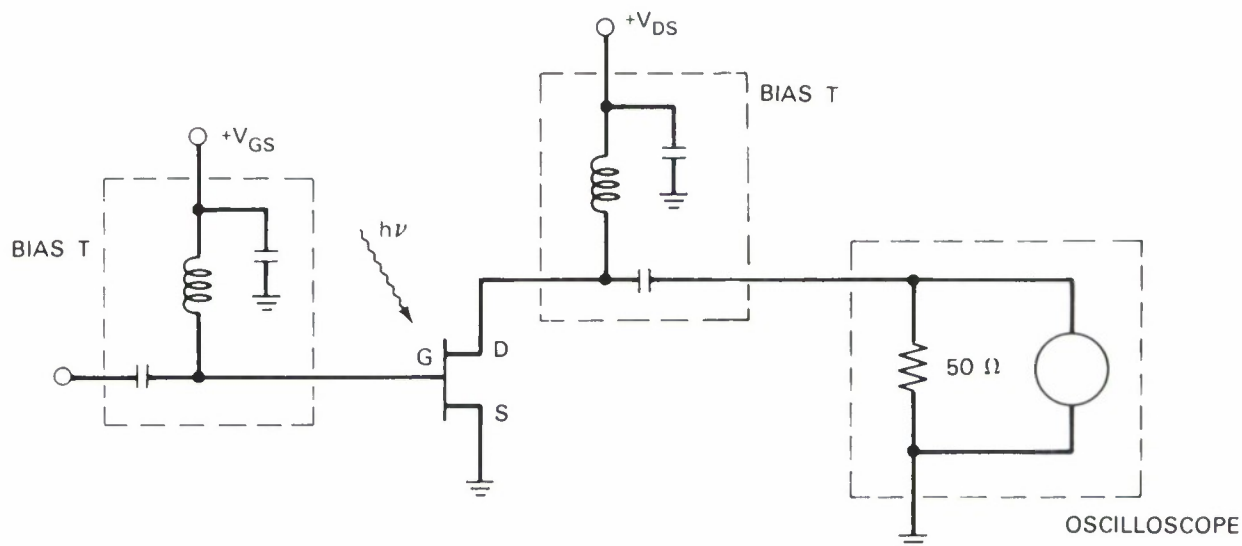


Figure 3-12. Schematic diagram of circuit used to bias packaged OPFETs.

The performance of the MGS OPFETs was found to depend strongly on bias conditions. For two-terminal (i.e., open gate) operation, the time response was very poor, with the signal exhibiting a tail that persisted long after the termination of the laser pulse. In the three-terminal configuration, as the negative gate bias (V_{gs}) was increased at fixed drain current (I_{ds}), the fall time initially decreased but the peak signal also decreased. Both effects are illustrated by Figure 3-13, which shows response curves obtained for our best device at $V_{gs} = -1.0, -1.25$, and

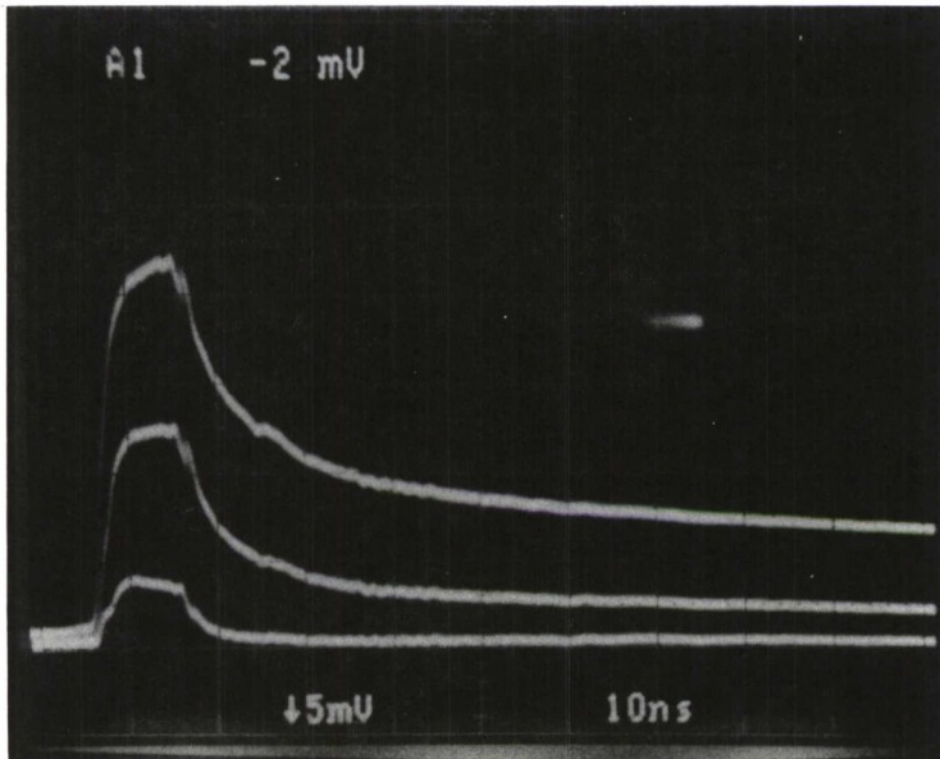


Figure 3-13. Pulse response of packaged OPFET for gate bias values (from top to bottom) of -1.0, -1.25, and -1.5 V.

-1.5V. Increasing V_{gs} above -1.5V did not reduce the fall time any further. We are currently modeling the device operation in an attempt to account for these effects.

The best response curve that we have measured, which was obtained for the device of Figure 3-13, is shown on an expanded time scale in Figure 3-14. The 0- to 100-percent rise time is 5ns and the fall time is approximately 10ns. The bias conditions were $V_{gs}=-1.4V$, $V_{ds}=0.2V$, and $I_{ds}=1.9mA$.

G.W. Turner
H.K. Choi

G M. Metze
T.H. Windhorn

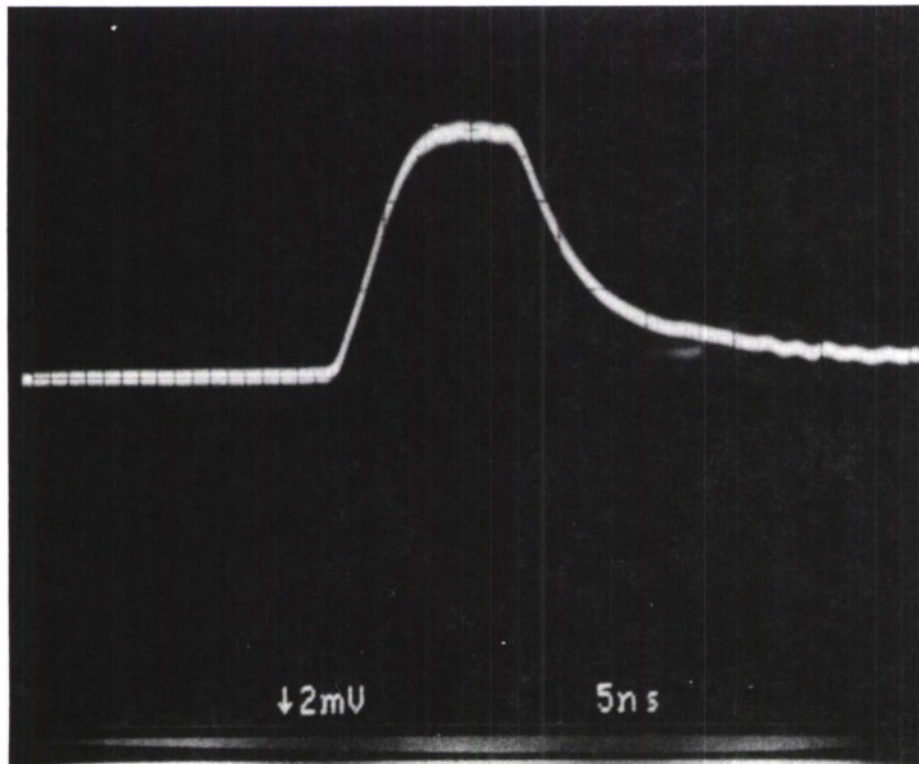


Figure 3-14. Fastest pulse response obtained for a packaged OPFET (gate bias is -1.4 V).

REFERENCES

1. J.C.C. Fan, B-Y. Tsaur, and M.W. Geis, *J. Cryst. Growth* **63**, 453 (1983).
2. M.W. Geis, H.I. Smith, D.J. Silversmith, and R.W. Mountain, *J. Electrochem. Soc.* **130**, 1178 (1983).
3. For results of similar approaches, see M. Takai, T. Tanigawa, K. Gamo, and S. Namba, *Jpn. J. Appl. Phys.* **22**, L624 (1983); and T. Nishioka, Y. Shinoda, and Y. Ohmachi, *J. Appl. Phys.* **56**, 336 (1984).
4. Solid State Research Report, Lincoln Laboratory, M.I.T. (1984:3), p. 34.
5. C.K. Lam, Y.C. See, D.B. Scott, J.M. Bridges, S.M. Perna, and R.D. Davis, *IEDM Technical Digest* (1982), p. 714.
6. T. Shibata, K. Hieda, M. Sato, M. Konaka, R.L.M. Dang, and H. Iizuka, *IEDM Technical Digest* (1981), p. 647.
7. S. Zirinsky, W. Hammer, F. d'Heurle, and J. Baglin, *Appl. Phys. Lett.* **3**, 76 (1978).
8. R.P. Gale, J.C.C. Fan, B-Y. Tsaur, G.W. Turner, and F.M. Davis, *IEEE Electron Device Lett.* **EDL-2**, 169 (1981).
9. Y. Shinoda, T. Nishioka, and Y. Ohmachi, *Jpn. J. Appl. Phys.* **22**, L450 (1983).
10. T.H. Windhorn, G.M. Metze, B-Y. Tsaur, and J.C.C. Fan, *Appl. Phys. Lett.* **45**, 309 (1984).
11. H.K. Choi, B-Y. Tsaur, G.M. Metze, G.W. Turner, and J.C.C. Fan, *IEEE Electron Device Lett.* **EDL-5**, 207 (1984).
12. T. Ishida, T. Nonaka, C. Yamagishi, Y. Kawarada, Y. Sano, M. Akiyama, and K. Kaminishi, *IEEE Trans. Electron Devices* **ED-31**, 1988 (1984).
13. G.M. Metze, H.K. Choi, and B-Y. Tsaur, *Appl. Phys. Lett.* **45**, 1107 (1984).
14. R. Fischer, T. Henderson, J. Klem, W.T. Masselink, W. Kopp, H. Morkoc, and C.W. Litton, *Electron. Lett.* **20**, 945 (1984).
15. C. Baack, G. Elze, and G. Walf, *Electron. Lett.* **13**, 193 (1977).
16. J. Gammel and J.M. Ballantyne, *IEDM Technical Digest* (1978), p. 120.
17. W.D. Edwards, *IEEE Electron Device Lett.* **EDL-1**, 149 (1981).
18. N. Matsuo, H. Ohno, and H. Hasegawa, *Jpn. J. Appl. Phys.* **23**, L648 (1984).

4. MICROELECTRONICS

4.1 A 420 × 420 CCD IMAGER FOR GROUND-BASED SATELLITE SURVEILLANCE

Charge-coupled device (CCD) imagers have long been of considerable interest for ground-based satellite surveillance because of their superior sensitivity, response uniformity, metricity, stability, and lifetime compared with the vidicon-type camera tubes currently deployed in the GEODSS (Ground-based Electro-Optic Deep Space Surveillance) system. In support of the GEODSS program at Lincoln Laboratory we are currently completing fabrication of 420 × 420 pixel CCD imagers which will be used in field tests to compare CCD performance with that of existing camera tubes. In this report we describe the design features of the device and some initial test results.

A schematic diagram of the CCD is shown in Figure 4-1. The device uses a three-phase structure, is fabricated with three levels of polysilicon, and is front illuminated. The pixel size in

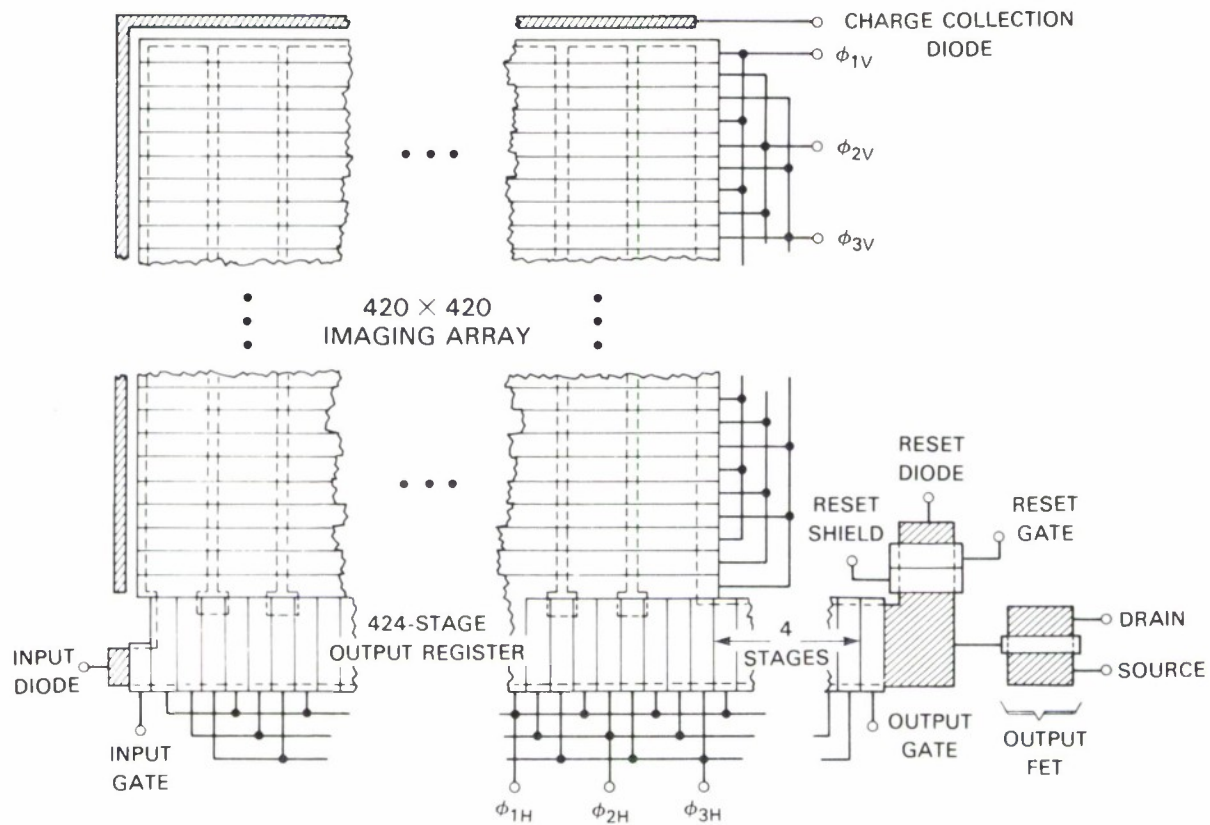
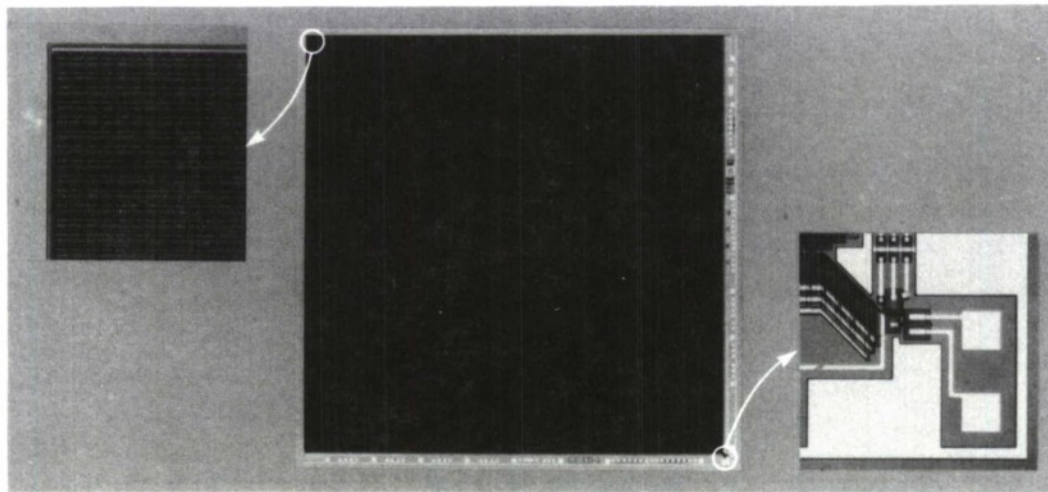


Figure 4-1. Schematic diagram of the 420 × 420 pixel CCD imager.

the array is $27 \times 27 \mu\text{m}$ with $4\text{-}\mu\text{m}$ channel stops (shown as dashed lines) defining the pixel columns. For convenience in testing, the output register has an electrical input which can be used to evaluate the charge transfer efficiency (CTE) not only of the output register but also that of the imaging array. This is possible because the charge transfer direction is reversible in a three-phase structure, allowing charge to be launched from the output register into the array and transferred up the columns as well as down. This feature has proven to be a useful adjunct to imaging tests in locating and studying pixels that have poor CTE. A photograph of a completed device is shown in Figure 4-2. The total die size is $11.3 \times 11.3 \text{ mm}$.

One of the unusual design requirements of this device is that it be capable of being abutted to two other identical die on two of its adjacent sides. With this feature a focal plane array of four imagers with 840×840 resolution can be assembled. From Figure 4-2 it can be seen that the output register and all bonding pads and test circuits are located on the bottom and right sides of the die, leaving the top and left sides for abutment to the other imagers. To minimize optical dead space or "seam loss" between imagers the devices must be cut very close to the active area next to the abutting edges. Since such cuts may introduce enhanced generation current from damage, we have included a narrow collection diode running along the two affected edges to intercept such current.



PIXEL SIZE: $27 \times 27 \mu\text{m}$
IMAGING AREA: $11.3 \times 11.3 \text{ mm}$

Figure 4-2. Photograph of the 420×420 CCD imager together with detailed views of the upper left corner and the output detection circuit in the lower right.

Approximately 30 3-in. wafers have been fabricated to date, each containing 17 imager die. The yield of die free from gate-gate shorts and gate-substrate shorts is about 70 to 80 percent. This is a high figure for such a large device, and can be attributed to some extent to the three-phase, triple poly process. Dynamic tests with optical and electrical inputs have been performed, and the result of an imaging test is shown in Figure 4-3. The CCD integration time was 0.8 s, after which the signal was clocked out at a 1-MHz data rate and displayed on a monitor. The image can be seen to be free of blemishes (regions of excess dark current) and other obvious defects. The yield of such very high quality devices is low, as one would expect for a device of this size, and currently averages only a few percent.

B.E. Burke
R.W. Mountain



Figure 4-3. Monitor photo showing the output signal resulting from an image projected onto the CCD.

4.2 SAW/FET WIDEBAND PROGRAMMABLE FILTER

In a previous report¹ we described the design and performance of a FET-programmable SAW transversal filter (SAW/FET) with a bandwidth of 50 MHz. This report details the design, fabrication, and performance of the FET chip.

The sampling fingers, nMOS programming circuitry, and spacer rails are fabricated on a 6.5×4.9 -mm silicon chip (Figure 4-4). The chip area is dominated by the SAW sampling fingers, which dwarf the programming circuits running along the top and bottom. Except for extra processing required for the sampling fingers and spacer rails, the chip is fabricated using a standard self-aligned silicon-gate nMOS process. The minimum feature size is $5 \mu\text{m}$, except for the $3.75\text{-}\mu\text{m}$ sampling fingers. The additional processing required for the SAW/FET consists of a second metallization step for the SAW sampling fingers and an extra etching step to form the spacer rails for the air gap. These rails contact the SAW device outside the primary acoustic beam region, yet place the sensing fingers close above the SAW piezoelectric fields.

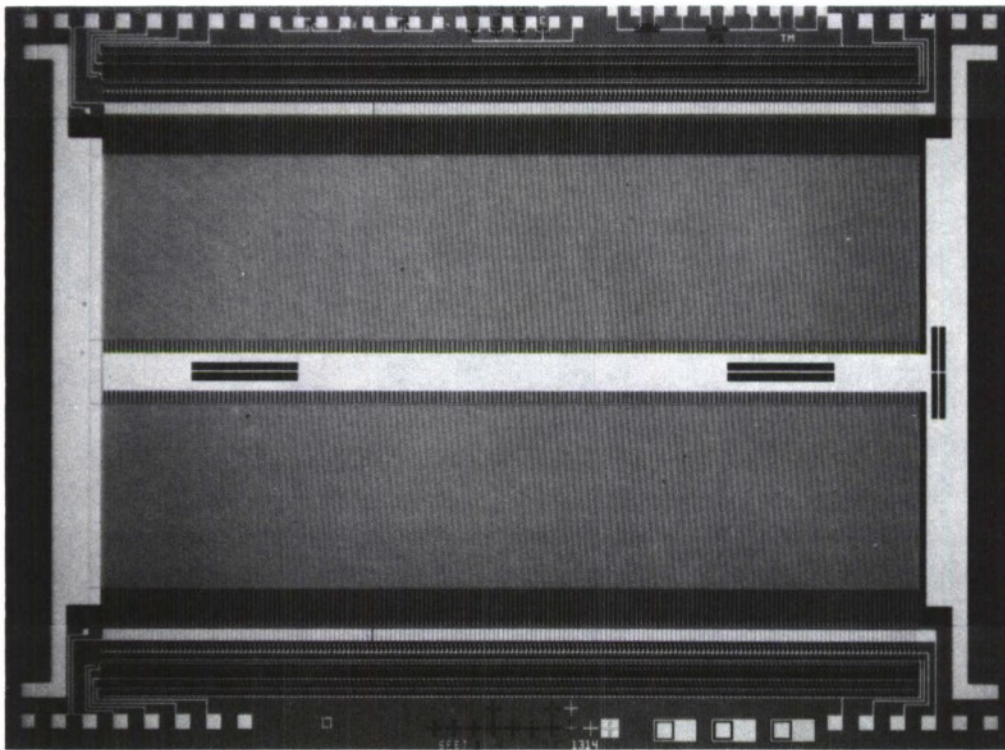
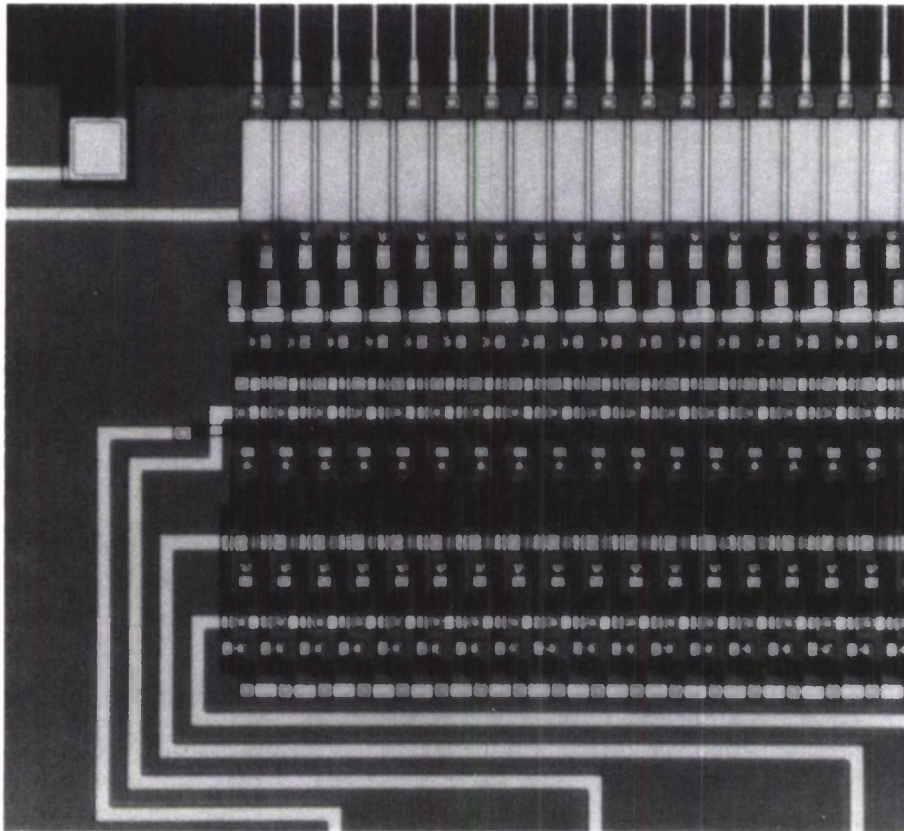


Figure 4-4. Photomicrograph of the SAW/FET chip containing dual 175-tap sampling arrays. Chip size is 6.5×4.9 mm.

A closeup view of one corner of the chip is shown in Figure 4-5, which shows the first several stages of the programming circuit. The sampling fingers can be seen at the top of this photomicrograph, with the output electrode below them, and the programming FETs can be seen directly below the output electrode. The remainder of the programming circuit consists of a standard dynamic MOS shift register² with the topology and layout modified to squeeze it into the 30- μm -wide space available for each stage. A schematic diagram of one stage of the programming circuit is shown in Figure 4-6.



150194-S

Figure 4-5. Magnified view of Figure 4-4 showing the lower left corner. The taps are on a 30- μm pitch.

The leakage current of the p-n junctions associated with the programming circuitry affects the programming rate and refresh time of the filter. The shift register in the programming circuit uses the parasitic capacitance associated with the gates of the transistors to store its state between successive clock cycles. All our shift registers function at clock rates as low as 1 MHz, as required. Similarly, the tap weight of each finger is stored on the capacitor formed between the

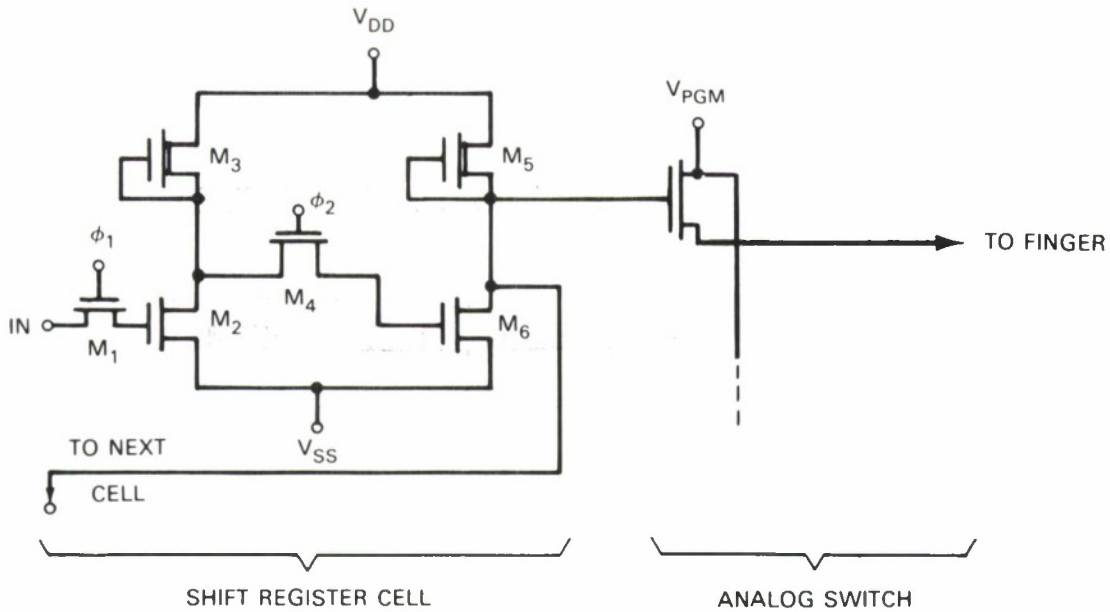


Figure 4-6. Schematic diagram of one stage of the programming circuit.

finger and the substrate, and excessive junction leakage current will de-program the fingers. We have measured the storage time of the fingers to be around 1 s at room temperature, which is more than adequate for our application.

D.L. Smythe

4.3 ETCHED-EMITTER SILICON PBT

Silicon permeable-base transistors (Si PBTs) have been fabricated which exhibit a small-signal short-circuit unity-current-gain frequency, f_T , of over 20 GHz. This compares favorably with device results using the most advanced high-speed silicon technologies, including submicrometer gatelength MOSFETs and super self-aligned bipolar transistors. The intrinsic f_T of nearly 30 GHz indicates this device should be useful as a high-speed switch.

We have previously reported results on etched-collector Si PBTs (Reference 3) [Figure 4-7(b)] which utilize a 50-nm-thick W base grating deposited at the bottom of a 320-nm-period etched-groove structure in silicon. The f_T for these devices was limited to about 10 GHz due to parasitic capacitances associated with the base shorting bar and base bonding pad. Here we report the results of etched-emitter Si PBTs [Figure 4-7(c)] fabricated using the same technology as the etched-collector Si PBTs with the addition of a shallow As implant for ohmic (emitter) contact.

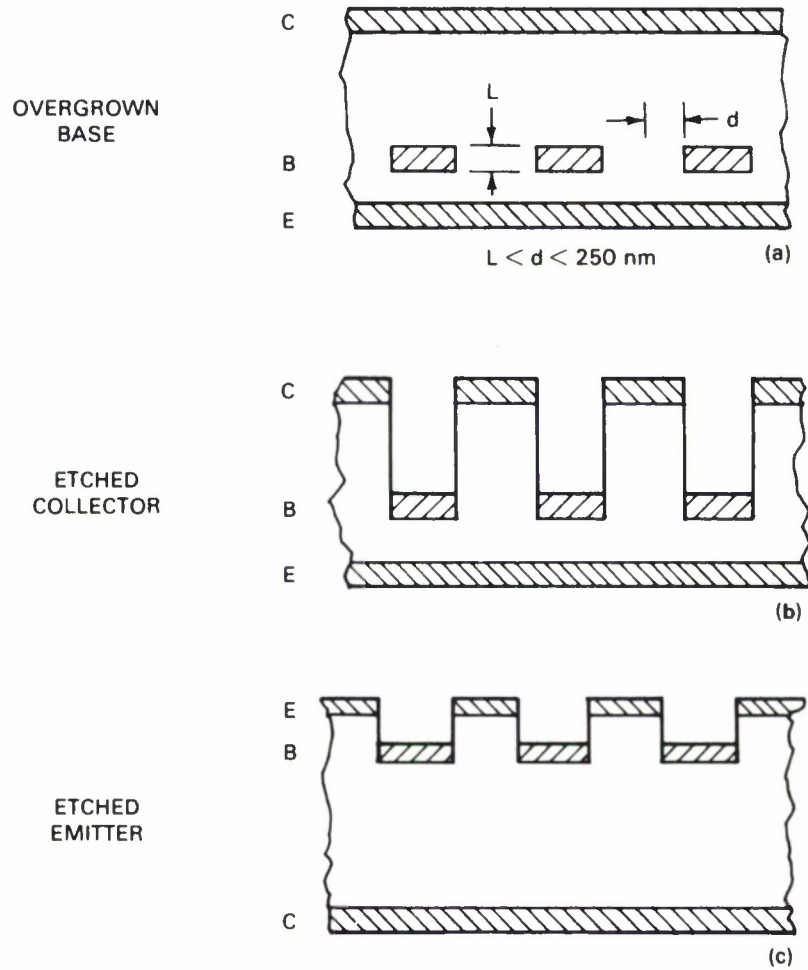


Figure 4-7. Three PBT configurations: (a) encapsulated-base, (b) etched-collector and (c) etched-emitter. The base grating periodicity and metal thickness are $4d$ and L , respectively.

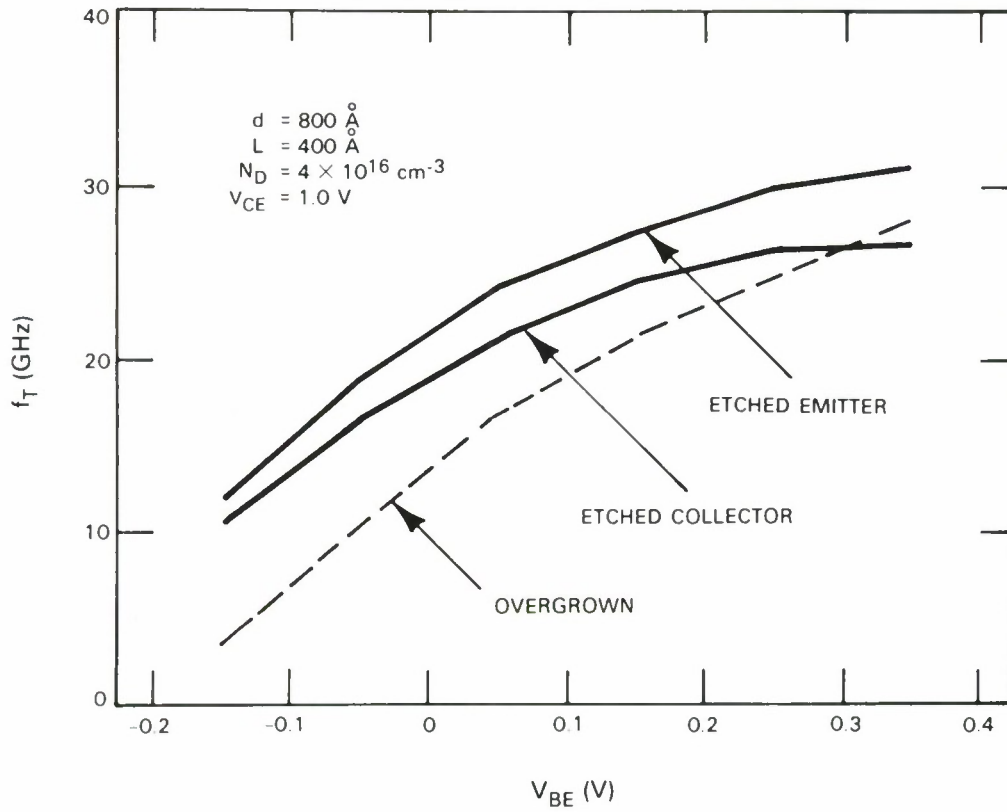


Figure 4-8. The unity short-circuit current-gain frequency f_T as a function of V_{BE} for the three devices of Figure 4-7.

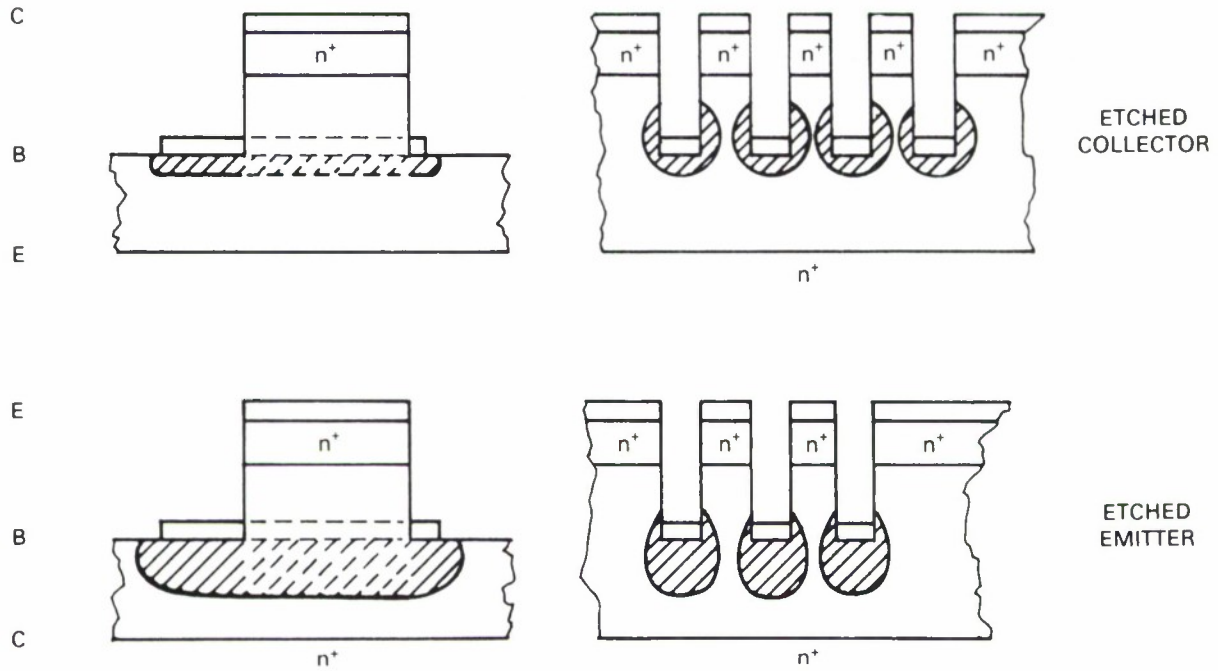


Figure 4-9. Comparison of the extent of the depletion region surrounding both the intrinsic and extrinsic base regions of the device when biased as an etched-collector or etched-emitter PBT.

Figure 4-8 is a comparison of the predicted intrinsic f_T vs base-to-emitter potential obtained by numerical solutions⁴ for the three PBT geometries shown in Figure 4-7. This result shows the etched-emitter device to have a higher intrinsic f_T than either the etched-collector or overgrown base devices. This is because the dominant capacitance for all three geometries, the base-to-emitter capacitance, C_{BE} , is significantly lower in the etched-emitter configuration due to removal of semiconducting material on the emitter side of the base. In addition, the parasitic capacitance associated with that part of the base metal outside the active area is also lower for the etched-emitter version because of the way in which the device is biased as shown in Figure 4-9. For the etched-emitter device the large positive bias on the substrate (collector) produces a large depletion region extending under the base contact outside the active area. This results in a lower parasitic capacitance for the etched-emitter device compared with an equivalent etched-collector device. The combined effect of a higher intrinsic f_T and an effectively lower parasitic capacitance should result in larger device f_T for the etched-emitter device.

Figure 4-10 shows the measured experimental results, where the common emitter current-gain vs frequency is plotted for our best etched-emitter and etched-collector devices to date. For the etched-emitter device f_T is at least 20 GHz.

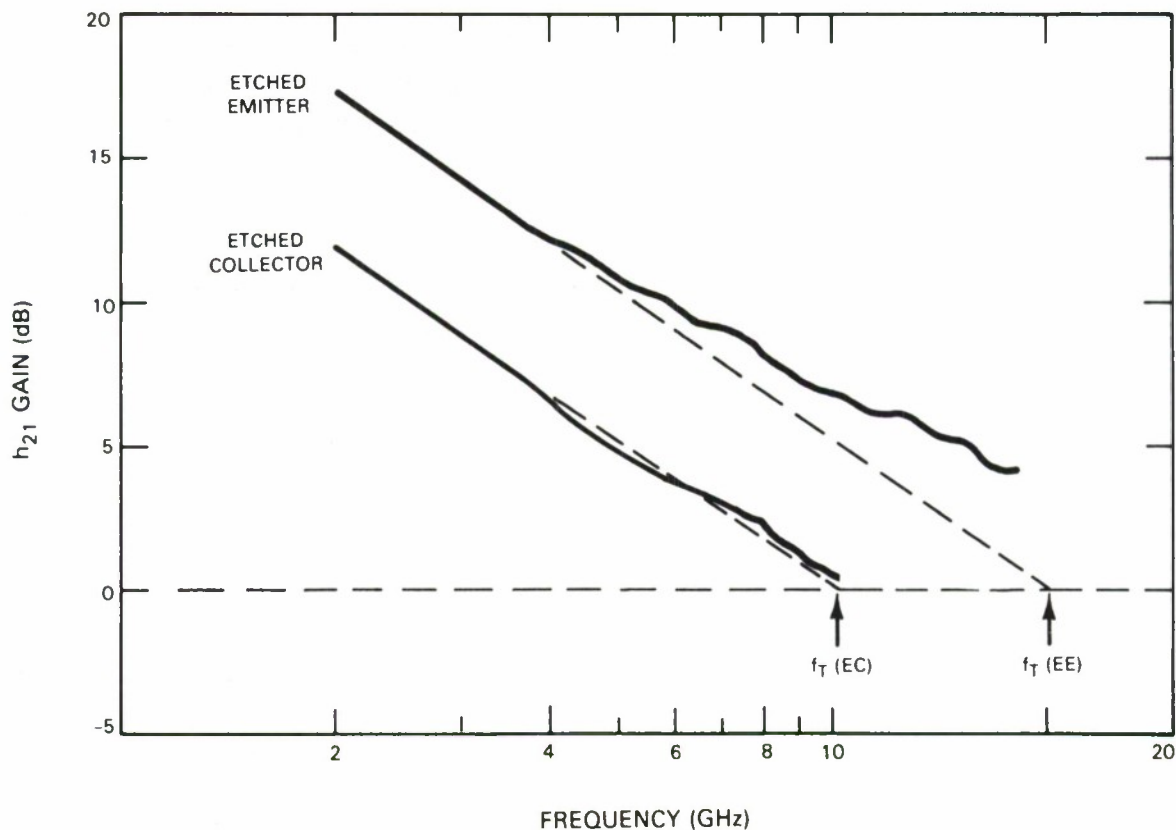


Figure 4-10. Common emitter current-gain vs frequency for the best etched-emitter and etched-collector devices.

Despite the higher f_T for the etched-emitter device, the best f_{max} obtained thus far is only 15 GHz compared to over 20 GHz for the etched-collector device. This is a result of the slightly higher collector-to-base capacitance of the etched-emitter structure and an anomalously high emitter series resistance, R_s , caused by surface states on the etched-emitter sidewalls. At present R_s is a factor of 12 \times higher for the etched-emitter device. Preliminary experiments indicate that passivation of the exposed sidewalls can be accomplished through the use of a dielectric such as Si_3N_4 or SiO_2 . The subsequent reduction in R_s should result in an f_{max} for the etched-emitter device that is about twice as large as that of an equivalent etched-collector device.

D.D. Rathman

4.4 LINEWIDTH CONTROL WITH MASKED ION-BEAM LITHOGRAPHY USING STENCIL MASKS

Previously, masked ion-beam lithography (MIBL) has been used to demonstrate high resolution and short exposure times in a proximity printing system.⁵ We report here the superior linewidth control which MIBL can achieve compared with optical lithography, when stencil masks are used. (We define good linewidth control as the ability to produce lines of small variation in width under a wide range of processing conditions.) In contrast to MIBL, fabrication of submicrometer features using optical lithography is limited both by poor image sharpness and by pattern-dependent biases.

Figure 4-11 compares the image sharpness from optical exposures reported by Rosenbluth⁶ to the image sharpness obtainable with MIBL using stencil masks. In the case of the optical exposure, the diffraction blurred image will result in large variations in the developed linewidth as a function of small changes in exposing dose and development conditions. The two effects which degrade contrast in the case of MIBL are beam divergence, which amounts to at most a 100-Å blur at the pattern edge, and ion scattering at the perimeter of the transmission holes in the stencil mask, which produces a very diffuse background similar to a mild and long-range proximity effect.⁷

Clean silicon wafers were spin coated with 3000 Å of PMMA resist, baked, and exposed with a 50-keV proton beam through a 1-μm-thick, silicon nitride stencil mask. We measured the variation in linewidths of the nominal 0.65- and 2.35-μm lines of the test pattern, both by an optical linewidth measurement system and by measuring micrographs taken using a scanning electron microscope (SEM). Where micrographs were used, the linewidth value was determined from several independent measurements which were made with reference to the periodicity of the test pattern. The measurement uncertainty was ±500 Å for the 2.35-μm lines and ±250 Å for the 0.65-μm lines. The accuracy of the optical instrument is specified to be 500 Å. In our experiments the standard deviation for the measurements was typically less than 500 Å for both sets of lines.

The exposing dose of 50-keV protons was varied from a minimum of 1.4×10^{13} ions/cm², which was required to completely develop the PMMA in 30 s in its normal positive resist response, to a maximum of 3.5×10^{14} ions/cm², which is high enough to cross-link the PMMA and achieve a negative resist response. Figure 4-12 graphs the measured linewidths as a function of exposing dose for both sets of lines. To within the accuracy of our measurements there is no significant variation in linewidth with respect to dose. The profiles of the resist were equally consistent with the exception of the cross-linked PMMA.

With ion-beam lithography using stencil masks, the insensitivity of the linewidths to large variations in dose allows very close control of pattern dimensions. Such control and large process latitude at submicrometer dimensions should prove advantageous in the fabrication of VLSI circuits. However, the use of simple stencil masks does have limitations such as restrictions on pattern geometries. Even with these limitations, the high resolution and excellent linewidth control of stencil masks may find applications in critical lithography steps.

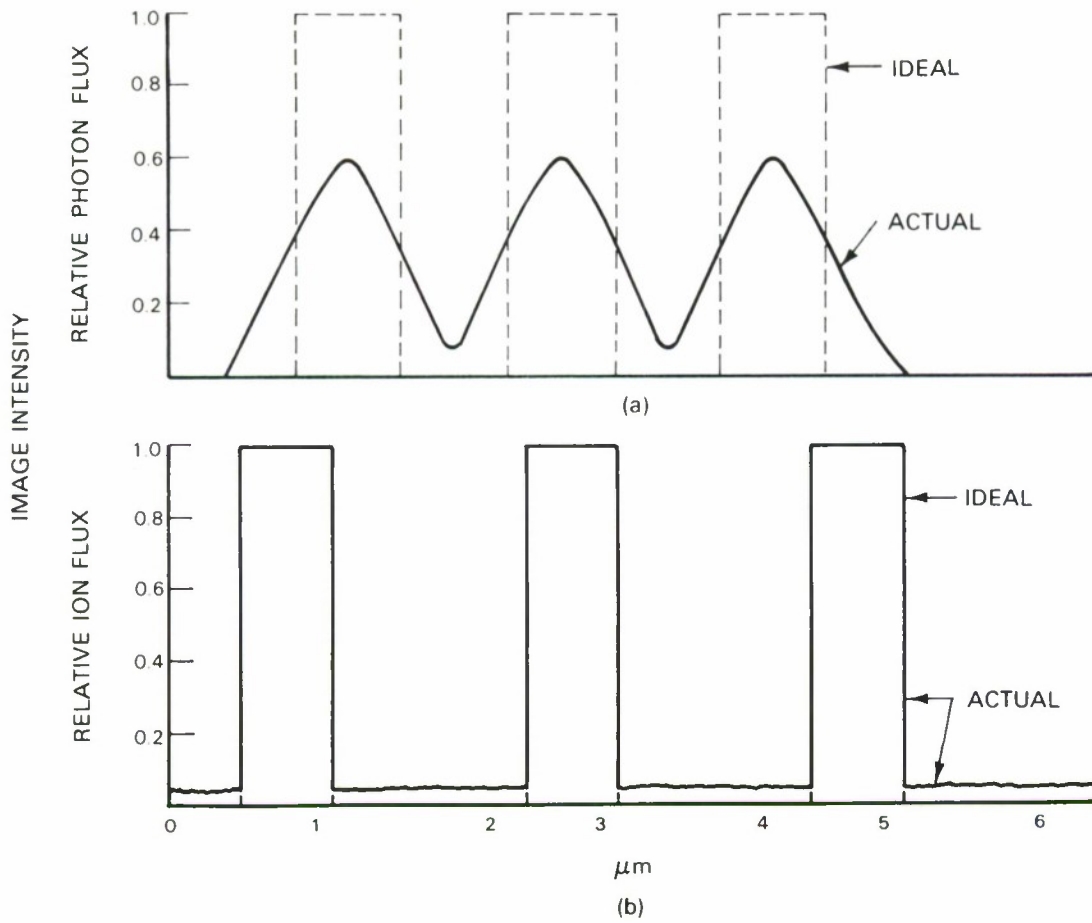


Figure 4-11. (a) Calculation of image intensity of an optical exposure system operating at a wavelength of 436 nm and with a 0.28 NA lens. The ideal image is three 0.75- μm -wide lines spaced 0.75 μm apart. The data for this graph were taken from Figures 3 and 4 of Reference 6. (b) Image intensity obtained when exposing 0.65- μm -wide lines on 2- μm centers with masked ion-beam lithography using a stencil mask. The only deviation from the ideal image is a background exposure level of approximately 3 percent, and slight taper (imperceptible on graph) of the line edges.

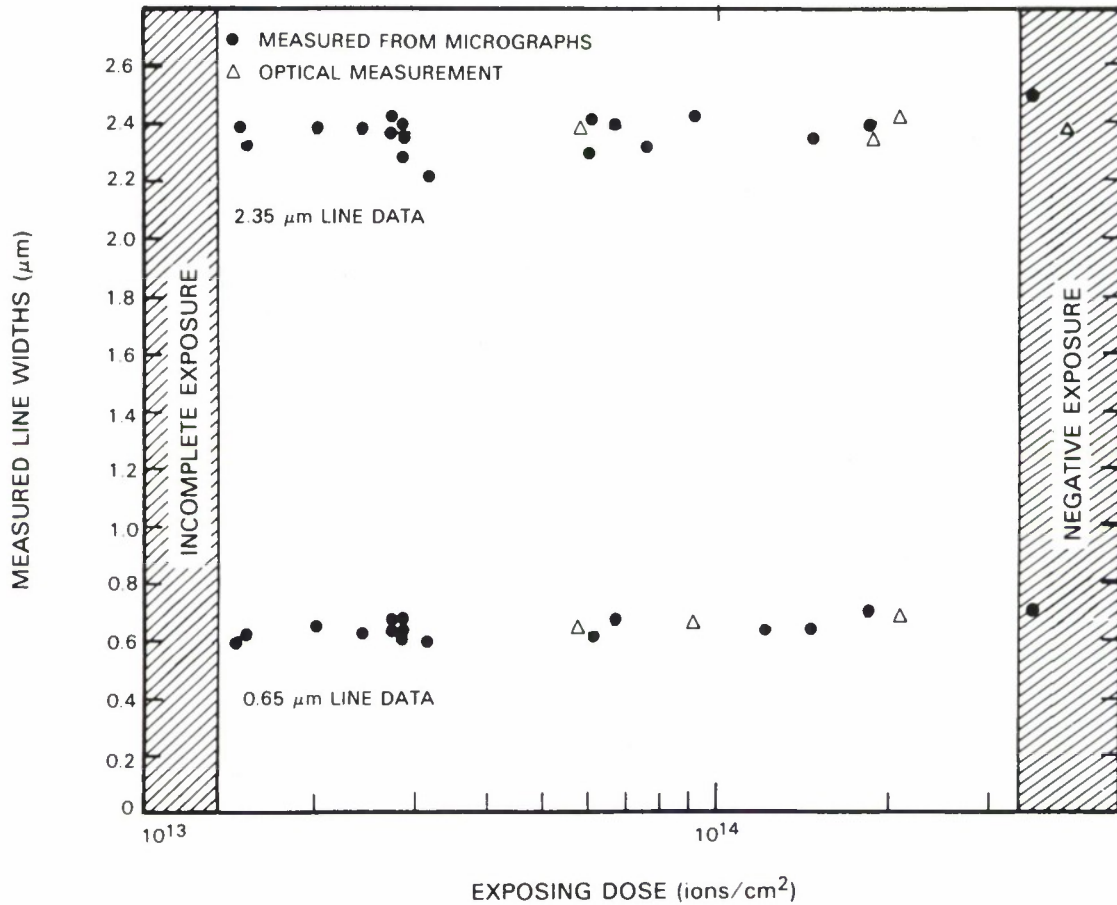


Figure 4-12. Plot of measured linewidths for 2.35- and 0.65- μm -wide lines. The dots are data points obtained from measuring SEM micrographs and the triangles are data points taken with the optical linewidth measuring instrument.

The use of a grid support stencil mask which replaces the completely open transmission areas with a matrix of small holes, eliminates many of the restrictions of stencil masks. Grid support masks, however, introduce factors which may affect linewidth control. The linewidth control and process latitude of grid support masks will be the subject of other publications.⁷

J.N. Randall
E.I. Bromley
N.P. Economou

4.5 SOLID-STATE SUBMILLIMETER HETERODYNE RADIOMETER

We have developed a solid-state submillimeter-wave radiometer which we have used to measure the rotational temperature of the H₂O transition at 557 GHz ($l_{10} \leftarrow l_{01}$) in a water vapor jet expanding into a high-vacuum chamber. Key advances in this radiometer are its high sensitivity, stability, compactness, and low operating power requirement.

A block diagram of the heterodyne radiometer is shown in Figure 4-13. The local oscillator (LO) of the radiometer is based on the submillimeter-wave oscillator chain described earlier,⁸ with the substitution of a 50-mW InP Gunn oscillator as the fundamental source at 92.6 GHz. The signal from this device was tripled in frequency by a GaAs Schottky varactor diode, then fed by waveguide to a frequency doubler, operating as a harmonic mixer.

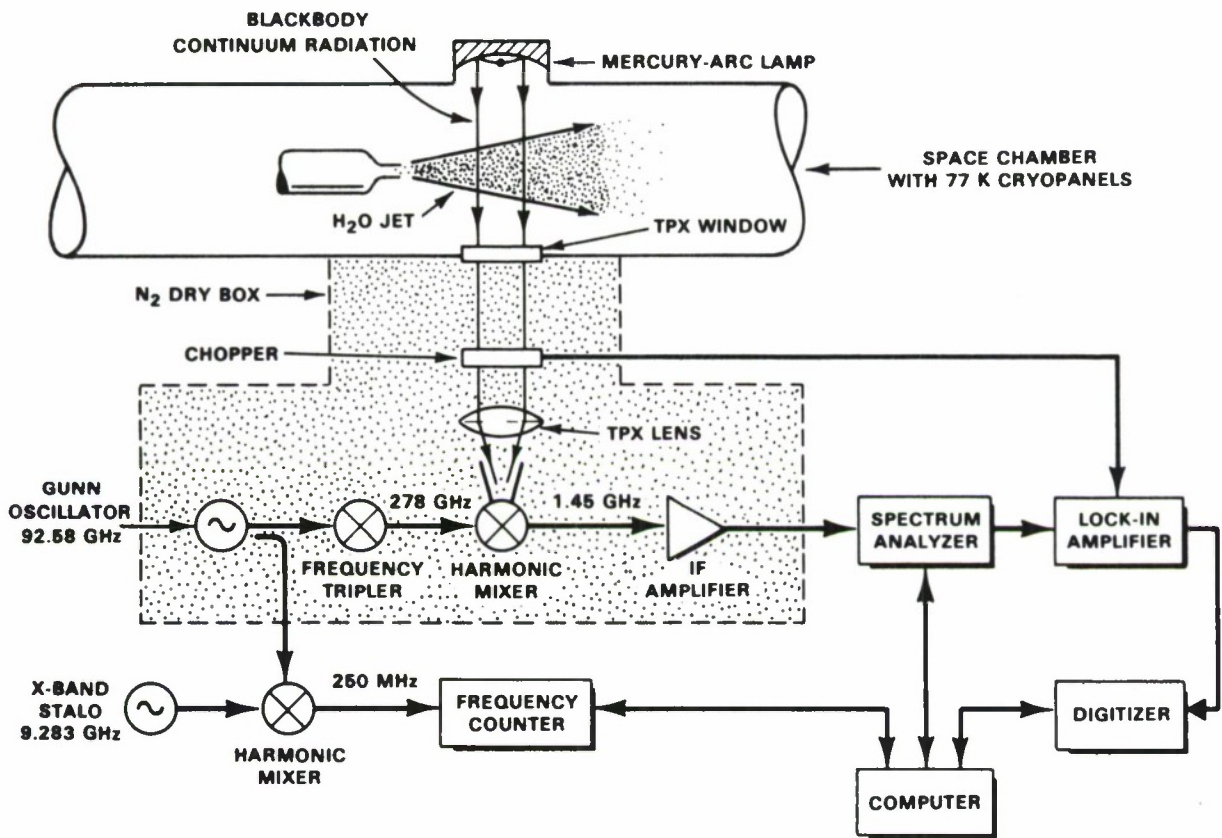


Figure 4-13. Block diagram of 557-GHz heterodyne radiometer.

The harmonic mixer combined the tripled Gunn signal with the chopped RF signal containing the spectral information to yield an intermediate frequency (IF) at 1.45 GHz. This IF signal was passed through a digitally controlled bandpass filter (in the spectrum analyzer), synchronously detected, digitized, and recorded by computer. The frequency resolution of ~ 600 kHz was limited by the sextupled frequency jitter of the free-running Gunn oscillator. A correction was made for the Gunn's frequency drift by a tracking filter loop that included an X-band stalo, harmonic mixer, frequency counter, bandpass filter, and computer.

With a receiver noise temperature of 8000 K (DSB), a predetection bandwidth of 300 kHz and an integration time of 3 s, a temperature resolution of 8 K was possible. Other tests have shown the receiver noise temperature to be below 4500 K (DSB) at slightly different frequencies.

The radiometer was used to repeat the space chamber water jet spectroscopy experiment that was previously carried out with a laser⁹ LO and a carcinotron¹⁰ LO. The present radiometer was exceedingly stable, so that the water vapor line could be traced out reproducibly with a resolution of ~ 600 kHz and a $S/N > 20$.

Figure 4-14 shows the H₂O absorption line measured against a Hg arc continuum with the radiation transverse to the flow axis at 200 nozzle diameters downstream from the nozzle and an input water flow rate of 0.5 g/s. The prominent self reversal appears to be due to the fact that

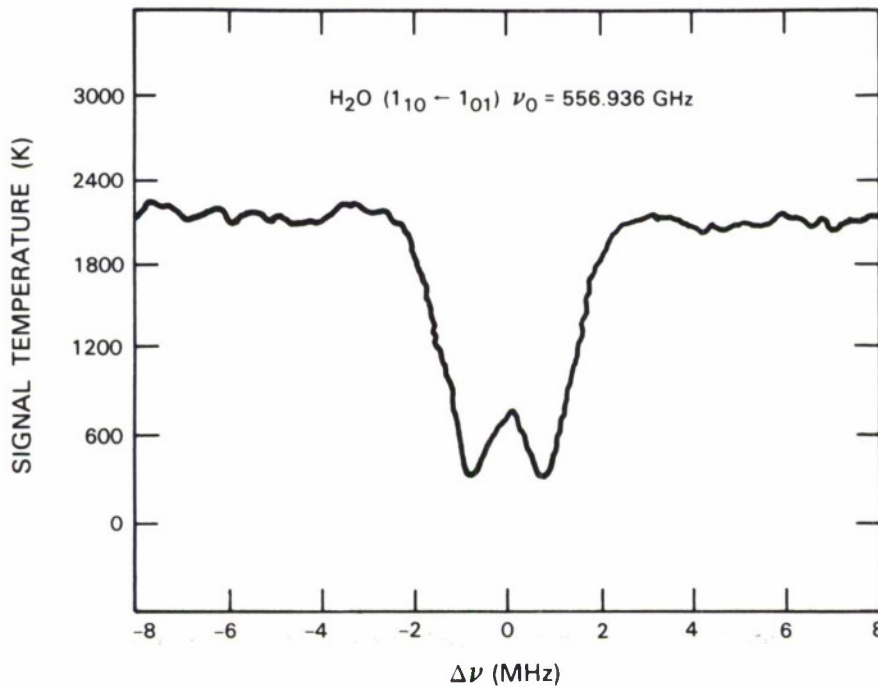


Figure 4-14. Absorption line of H₂O jet illuminated by Hg arc lamp under conditions which caused a self reversal around the center of the line.

the jet contained Doppler shifted regions of varying optical depth and temperature. The shape and magnitude of the self reversal were sensitive to the particular H_2O flow rate and the distance downstream from the nozzle, as observed in the earlier experiment¹¹ with the laser LO.

These results represent a significant improvement in our capability in submillimeter radiometry.^{9,10} The sensitivity has been increased by a factor of 3, and the stability and frequency resolution have been improved by factors of about 10 and 2, respectively. The weight of the front end of the receiver has been reduced to <3 kg and the DC power consumption was only about 3 W.

This experiment shows that a compact LO requiring low input power could be developed for a satellite-based radiometer. NASA is proceeding with this concept for submillimeter astronomy, and other space-based applications can be envisioned.

J.A. Taylor G.F. Dionne (Group 33)
P.E. Tannenwald J.F. Fitzgerald (Group 33)
N.R. Erickson*

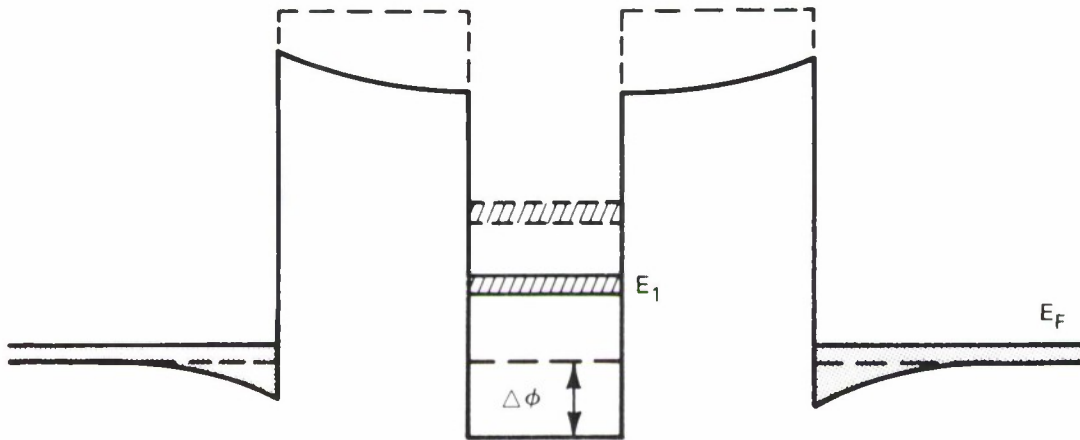


Figure 4-15. Electron energy as a function of position in a quantum well structure with positive charge in the barriers and the electrons outside the barrier well region. The dashed lines show the conduction band in the absence of ionized centers.

*Five College Radio Astronomy Observatory, University of Massachusetts, Amherst.

4.6 PERSISTENT PHOTOCONDUCTIVITY IN QUANTUM WELL RESONATORS

Resonant tunneling structures (quantum well resonators) have recently been shown to possess some intriguing characteristics, including high-speed charge transport ($\tau < 10^{-13}$ s) and broad regions of negative resistance that can be used to produce oscillations at microwave, and perhaps higher, frequencies.^{12,13} These heterostructure devices contain GaAs-AlGaAs interfaces so that carriers in the AlGaAs diffuse to the GaAs with lower bandgap, leaving behind an ionized impurity, and establish a dipole layer across the interface. In addition to hydrogenic impurities, it is well known¹⁴ that in AlGaAs, electron traps called DX centers exist which, once optically ionized, remain so for long times at low temperatures, giving rise to a persistent photoconductivity. The effect of the presence of positively charged centers in the barriers on the electron energy is shown by the solid lines in Figure 4-15, while the dashed line shows the energy in the absence of ionized centers. Here the basic tunneling structure is our usual GaAs quantum well formed by two surrounding GaAlAs barriers. Current peaks occur when the voltage across the double-barrier region is roughly equal to $2E_i/e$, where E_i is one of the allowed energies, measured from the Fermi level of electron motion normal to the barriers for carriers confined to the well. In our structures only one level occurs, which is marked E_1 in Figure 4-15.

In a typical experiment the sample was cooled to 20 K in the dark. The sample was then exposed to light at a given wavelength, and an I-V curve was taken. I-V curves were recorded after every exposure, to produce a sequence of curves, some of which are shown in Figure 4-16(a). Aside from the curve taken before exposure, successive curves have ten times greater exposure. The 100 Q curve has had nearly all the DX centers ionized. After the persistent photoconductive effect had saturated, the sample was warmed to room temperature and re-cooled for another experiment at a different wavelength.

The effects observed in Figure 4-16 can be explained by the model shown in Figure 4-15 and a calculation of the I-V curves at finite temperature in a way similar to that suggested by Tsu and Esaki,¹⁵ except that accumulation and depletion regions are included. Figure 4-16(b) shows I-V curves calculated using this model for the same relative exposures as the experimental curves of Figure 4-16(a) and the DX center density. The parameters used in the model were consistent with the growth constants of the structure as described above except that the temperature used in the model was 60 K rather than the physical temperature of the device of 20 K. The fact that little change in the I-V curves is seen below about 100 K supports this evidence that some electron heating is occurring. The agreement with the observed curves is excellent considering the simplicity of the model. The current increase at high voltage is not completely understood. More details of this model will be described in the future.

T.C.L.G. Sollner C.A. Correa
H.Q. Le W.D. Goodhue

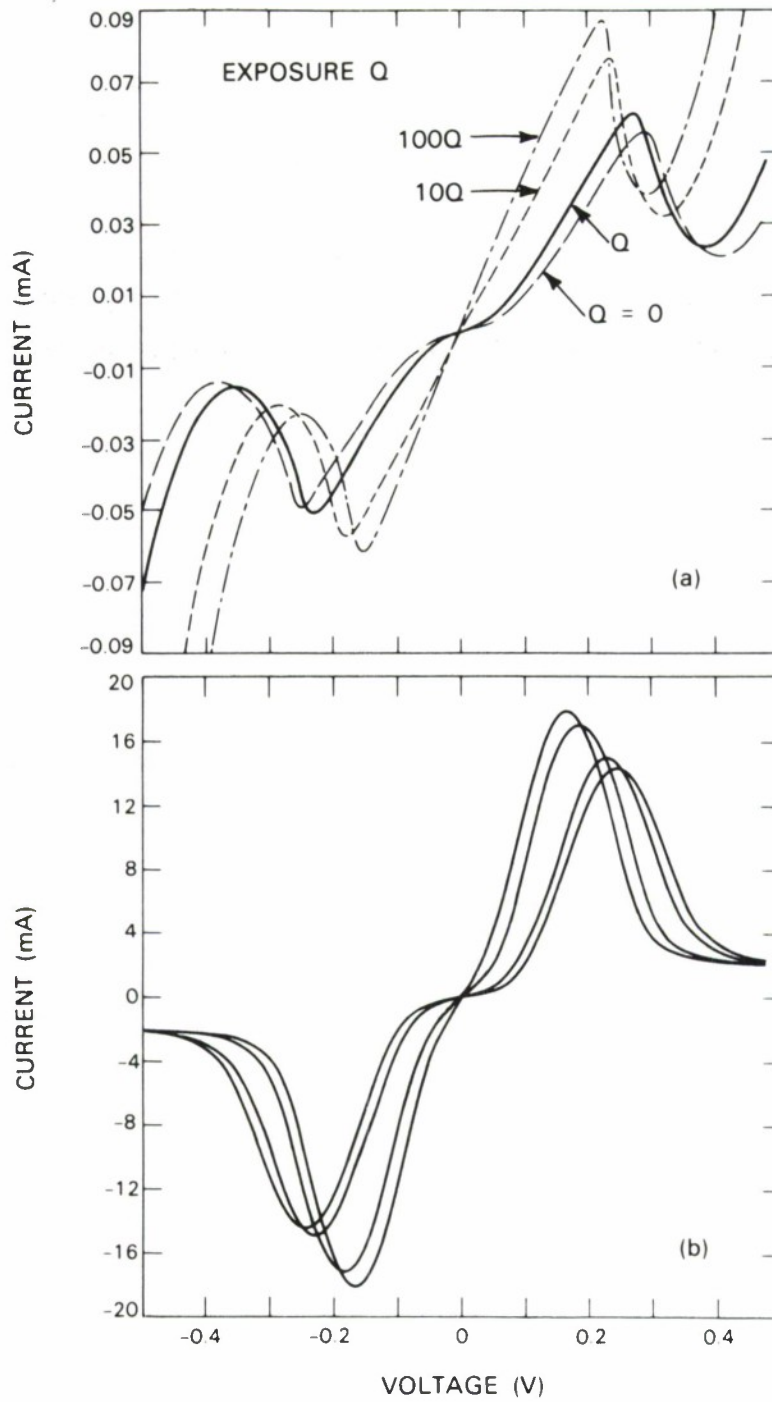


Figure 4-16. Observed (a) and calculated (b) I-V curves for the structure shown in Figure 4-15 for several exposures to 0.85- μm radiation. The long-dashed curve is unexposed, the solid curve has had an arbitrary exposure, Q, the short-dashed curve has exposure 10 Q and the broken curve has exposure 100 Q.

REFERENCES

1. Solid State Research Report, Lincoln Laboratory, M.I.T. (1984:3).
2. C. Mead and L. Conway, *Introduction to VLSI Systems* (Addison-Wesley, Reading, Massachusetts, 1980), p. 67.
3. D.D. Rathman, B.A. Vojak, D.C. Flanders, and N.P. Economou, Proc. 1984 Intl. Conf. on Solid State Devices and Materials, August 1984, pp. 305-308.
4. B.A. Vojak and G.D. Alley, IEEE Trans. Electron Devices **30**, 877 (1983).
5. J.N. Randall, D.C. Flanders, N.P. Economou, J.P. Donnelly, and E.I. Bromley, J. Vac. Sci. Technol. B., to be published.
6. A.E. Rosenbluth, D. Goodman, and B.J. Lin, J. Vac. Sci. Technol. **1**, 1190 (1983). Data for our Figure 4-1 taken from their Figure 4.
7. J.N. Randall, L.A. Stern, and J.P. Donnelly, to be submitted to Electron, Ion and Photon Beam Conference (EIPB), Portland, Oregon, May 1985.
8. Solid State Research Report, Lincoln Laboratory, M.I.T. (1982:2), p. 61, DTIC AD-A122252.
9. G.F. Dionne, J.F. Fitzgerald, T-S. Chang, M.M. Litvak, and H.R. Fetterman, Intl. J. Infrared and Millimeter Waves **1**, 581 (1980).
10. G.F. Dionne, H.R. Fetterman, N.R. Erickson, C.D. Parker, and J.F. Fitzgerald, IEEE J. Quantum Electron. **QE-20**, 188 (1984).
11. G.F. Dionne, M.M. Litvak, J.A. Weiss, J.F. Fitzgerald, and H.R. Fetterman, Appl. Phys. Lett. **42**, 862 (1983).
12. T.C.L.G. Sollner, W.D. Goodhue, P.E. Tannenwald, C.D. Parker, and D.D. Peck, Appl. Phys. Lett. **43**, 588 (1983).
13. T.C.L.G. Sollner, P.E. Tannenwald, D.D. Peck, and W.D. Goodhue, Appl. Phys. Lett. **45**, 1319 (1984).
14. R.J. Nelson, Appl. Phys. Lett. **31**, 351 (1977); or see D.V. Lang, R.A. Logan, and J. Jaros, Phys. Rev. **B19**, 1015 (1979).
15. R. Tsu and L. Esaki, Appl. Phys. Lett. **22**, 562 (1973).

5. ANALOG DEVICE TECHNOLOGY

5.1 *In situ* AMPLITUDE AND PHASE ADJUSTMENT OF SAW DEVICES BY LASER-PHOTOCHEMICAL ETCHING

The application of laser-direct writing¹ has been extended to *in situ* trimming of phase and amplitude characteristics of surface-acoustic-wave (SAW) reflective-array compressors (RACs) on LiNbO₃. The technique employs the photochemical etching of a phase-compensating metal film and a recently developed metal/cermet amplitude-compensating film. The process is labeled *in situ* because the etching is controlled by simultaneous electrical measurements of the device response.

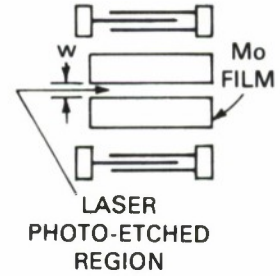
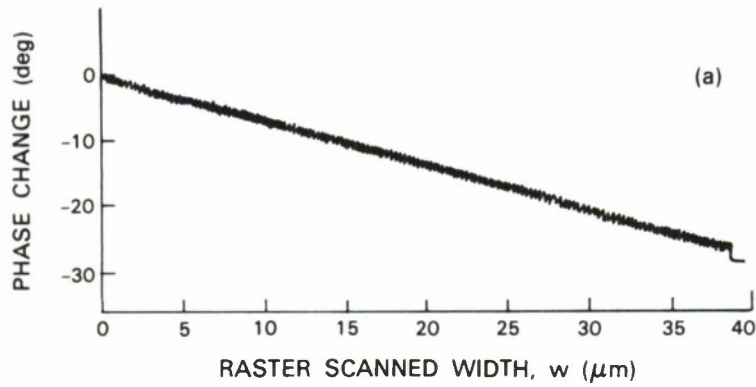
The motivation for *in situ* etching of RACs is prompted by limitations on yield and device performance with existing fabrication and compensation techniques. RACs are presently used to advantage in high-performance radar and communication systems; system requirements are imposing ever more stringent control of phase and amplitude.

Previously, phase compensation of RACs has been accomplished by defining a metal pattern in the region between the acoustic gratings.² Through the velocity change associated with its piezoelectric loading, the variable-width films adjust phase on a frequency-by-frequency basis to within approximately 2° rms of the desired characteristic. The additional photolithographic lift-off processing, however, perturbs the amplitude response somewhat and precludes finer phase adjustment. No amplitude-compensation technique, short of complete iteration of device fabrication with a modified groove-depth profile, has previously been demonstrated, and amplitude errors of 0.2 dB rms have been achieved only with painstaking process control. Generally, with the small quantities required for delivery, the yield has been limited to ~50 percent for a compensated device in a final package assembly.

We anticipate that application of the new methods described here when used for final correction of a fully packaged RAC will permit the production with improved yield of devices with an order-of-magnitude improvement of phase errors (0.1°) and amplitude errors (0.01 dB).

To date, laser processing of film structures on LiNbO₃ has been complicated by the extreme susceptibility of this substrate to damage by nonlinear optical absorption and by localized heating. To overcome this complication, a fast low-temperature reaction has been developed for etching molybdenum, an acceptable SAW-compensating film on LiNbO₃. The selection of molybdenum followed an extensive investigation of a number of candidate thin films and a variety of laser-activated etchant gases.

The basic configuration and the several methods for microchemical laser-direct writing have been described previously.³ An inverted optical microscope is used for focusing; positioning is by computer-controlled scanning of the device on a mechanical stage. In the present experiments a 0.25- μ m resolution is achieved by stepping the stage by this increment. Typically, 50 to 100 mW



YZ LiNbO₃ DELAY LINES

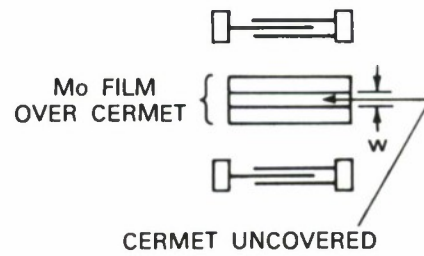
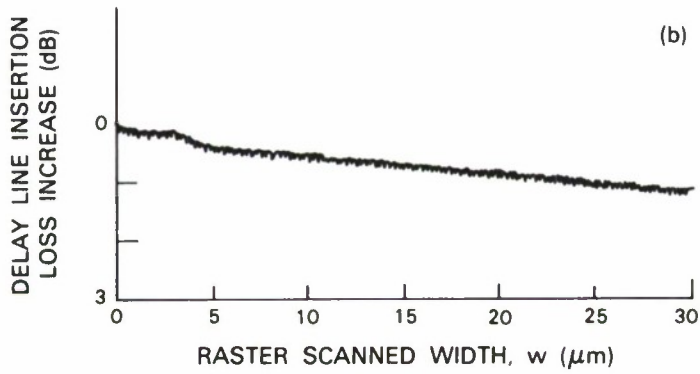


Figure 5-1. Laser microchemically etched test delay-line structures demonstrate monotonic change in (a) phase and (b) amplitude response. The Mo film between the delay-line transducers is continuously removed in a raster scan fashion to uncover 0.25- μm strips of (a) LiNbO₃ for phase compensation and (b) cermet for amplitude compensation.

of 488.0-nm light from a CW argon-ion laser is focused through a 5X refractive objective to provide a 2.5- μm spot size. The scan pattern is controlled by a PDP-11 computer according to a routine which, for these initial experiments, is determined off-line for the individual SAW-device substrate by an appropriate design and test algorithm on a separate computer. During final test and trimming, 50 to 500 Torr of the etch gas (most successfully Cl_2) is maintained above the fully bonded device via relatively minor modifications of the already vacuum-compatible SAW package. Although somewhat limited in these first experiments, test equipment at the scanning stage allows simple monitoring of the electrical response of the device under trim.

The chemical mechanism of the etching reaction is similar to that previously described for Cl_2 etching of Si (Reference 4). Briefly, the reaction is based on argon-ion laser dissociation of molecular chlorine and modest local heating of the Mo film in the resulting atomic chlorine atmosphere. The process is notable for its spatial resolution of better than 0.25 μm (Reference 5).

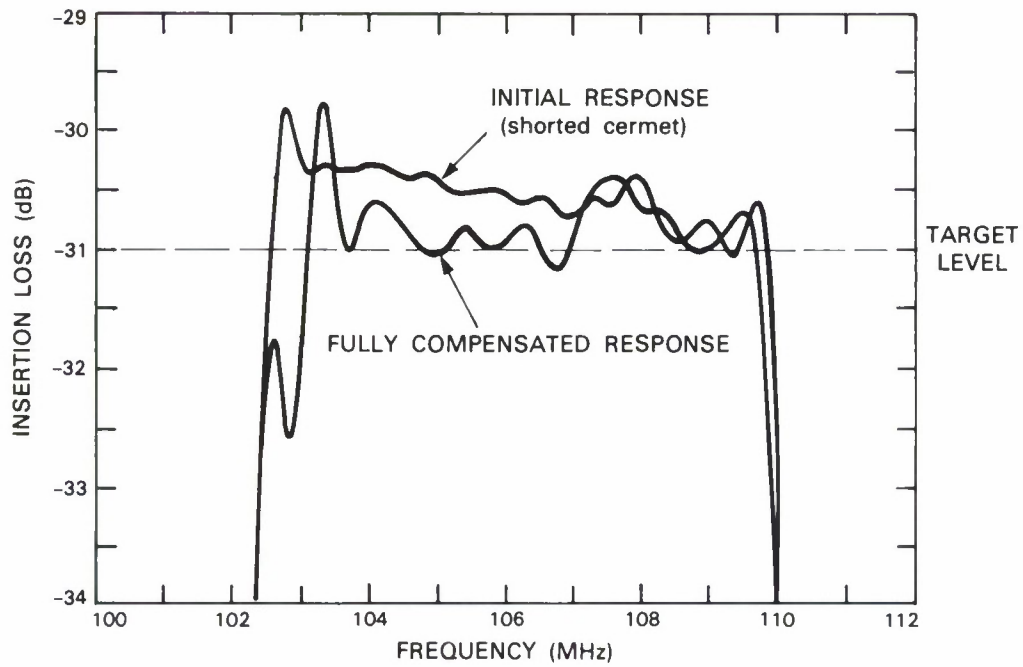
Two film combinations developed especially for laser-activated etching separately provide phase and amplitude trimming. Test delay lines with respective phase- and amplitude-compensating films are shown in Figures 5-1(a) and (b). Experimental results verify the expected resolution limits achievable for the process developed.

In each experiment Mo is removed in 0.25- μm strips by the focused laser spot as the substrate is scanned across the acoustic beam path. The scanning stage is incrementally stepped 0.25 μm in the direction of SAW propagation and returned across the full acoustic aperture. The cycle is repeated for uniformly continuous removal of Mo.

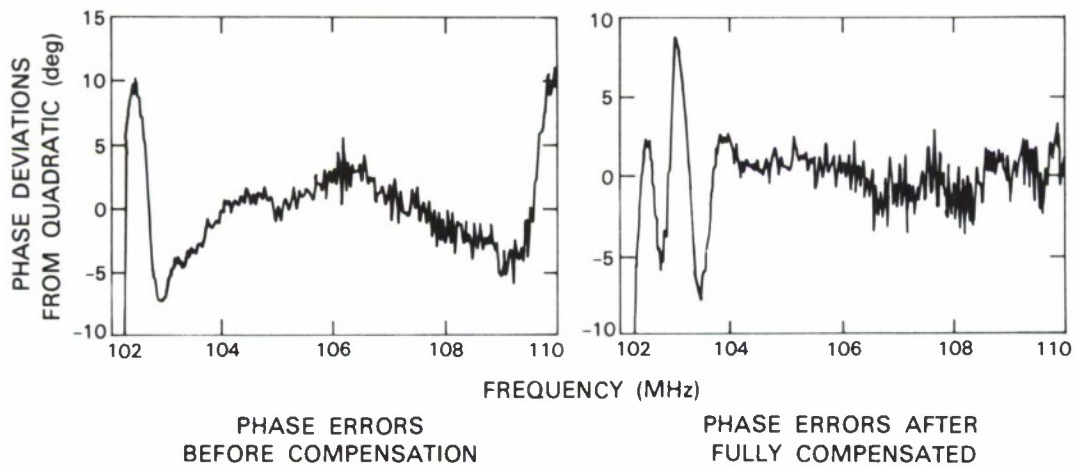
Removal of Mo from the LiNbO_3 surface resulted in a measured phase change of 0.15° for each 0.25- μm Mo strip etched. The results obtained in real time are shown in Figure 5-1(a). At the test frequency of 250 MHz, this is the expected phase change. The broadened trace is a result of transient local heating.

The thin-film combination used for amplitude trimming is shown in Figure 5-1(b). Cermet ($\text{Cr}/\text{Cr}_2\text{O}_3$) films are known to attenuate surface acoustic waves reproducibly.⁶ A conductive Mo film over the cermet renders the combination nonattenuating. Controlled removal of Mo occurs with no change in the desired attenuation characteristics of the underlying cermet layer. Etching Mo in 0.25- μm strips in order to uncover a region of cermet as schematically shown in Figure 5-1(b) results in a measured attenuation of 0.45 dB per wavelength. This is in good agreement with previously measured average values of 0.35 dB per wavelength for typical large-area films. The measured attenuation corresponds to a change of 0.01 dB at 250 MHz for each 0.25 μm of uncovered cermet.

Real-time trimming of amplitude and phase response of a test RAC was also demonstrated. To this end a featureless cermet strip ~ 1.6 mm wide was sputter-deposited in the 2.7-mm space between the RAC gratings during initial device fabrication. Subsequently, a wider (2.4-mm) Mo strip was e-beam evaporated over the cermet and adjacent LiNbO_3 surface. The device was mounted in its final vacuum-tight package and photochemically etched.



(a)



(b)

Figure 5-2. (a) Amplitude response and (b) phase deviations from quadratic response of the fully compensated RAC compared with the initial uncompensated device measurements and the target levels. The coupled amplitude/phase error at the low-frequency band-edge in the response measurements of the compensated RAC is the result of a large and inappropriate local amplitude correction.

The amplitude and phase responses of the thereby fully compensated RAC are compared to the uncompensated responses and the target levels in Figures 5-2(a) and (b), respectively. The overall amplitude tilt shown in Figure 5-2(a) is removed. Added across the band is an aggravated ripple. The result was expected: compensation was performed in an open-loop fashion using a simplistic algorithm to generate the amplitude and phase trim patterns. It was assumed that amplitude and phase corrections could be made independently on a point by point basis for each frequency measured. The approach is incorrect because amplitude and phase characteristics are coupled, and also an extended region of the grating contributes to the response at any one frequency. The full transfer function of the device must be considered, as described and demonstrated in an earlier paper.⁷

These preliminary experiments have demonstrated an amplitude correction technique suitable for RAC devices as well as a laser-activated photochemical total compensation process which is compatible with LiNbO₃ SAW substrates. Delay-line trim measurements have demonstrated 0.25- μ m resolution limits with the available apparatus, providing a 0.15° phase-trim and a 0.01-dB amplitude-trim capability at 250 MHz. The RAC trim experiment showed the process was feasible and indicated that a coupled amplitude-phase algorithm is required before full exploitation of the technique can be realized.

V.S. Dolat
D.J. Ehrlich

5.2 SUPERCONDUCTIVE CHIRP-TRANSFORM SPECTRUM ANALYZER

Dispersive acoustic delay lines have been employed in chirp-transform processors to perform rapid spectral analysis over instantaneous bandwidths of a few⁸ to a few hundred megahertz.^{9,10} Similar performance is projected for surface-wave acoustooptic spectrum analyzers.¹¹ Recently, a bulk acoustooptic spectrum analyzer with a bandwidth of 1 GHz, a frequency resolution of 50 MHz, and a dynamic range of 40 dB was demonstrated,¹² and Bragg cells with 2-GHz bandwidth were developed.¹³

Here we report the construction of a spectrum analyzer employing superconductive tapped electromagnetic delay lines, rather than acoustic delay media. Low-loss delay and accurate tapping functions are provided by planar niobium striplines on thin dielectric substrates. Unlike the acoustic devices, wide bandwidth with low loss is readily achieved with this approach. Delay time is currently constrained by substrate size, however, and thus the time-bandwidth products of the devices are modest compared to those of the more mature acoustic technology.

Chirp filters with bandwidths in excess of 2 GHz for pulse expansion and compression have been realized in the form of tapped electromagnetic delay lines.^{14,15} In order to achieve useful delay with low loss in a compact package, miniature stripline of superconducting niobium thin film is patterned on thin dielectric substrates. Two parallel lines, shown schematically in Figure 5-3, are coupled by a series of backward-wave couplers. Practical devices contain more than a hundred such couplers, although only four are shown in the figure. At each change in line separation s , a portion of the energy propagating from port 1 on the upper line is tapped out and

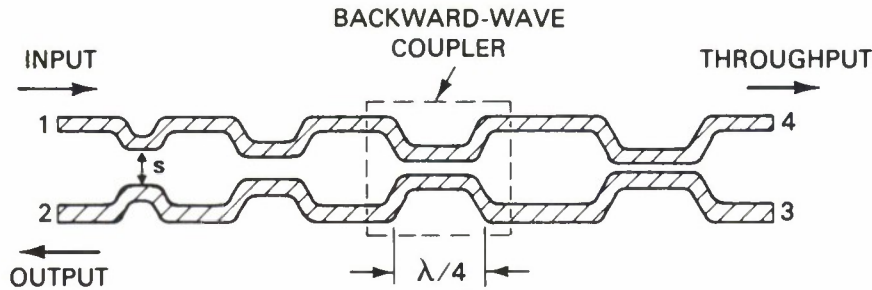


Figure 5-3. Chimp filter formed by cascading backward-wave couplers between adjacent electromagnetic delay lines.

128905-N-03

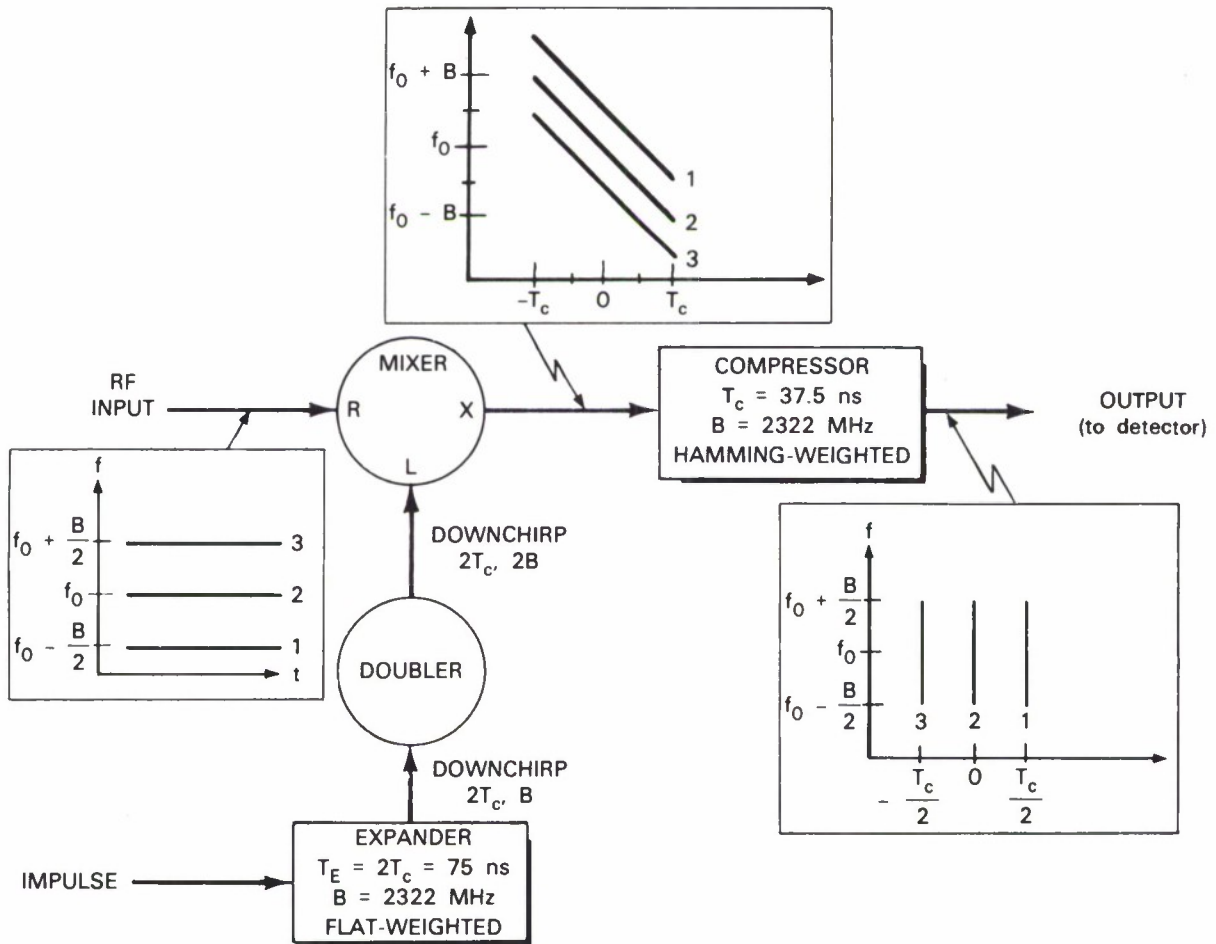
adds to a wave propagating toward port 2 on the lower line, a process similar in many ways to the coupling in a reflective grating. In the frequency domain, the coupled lines have a local resonant frequency which is inversely proportional to the tap spacing. When the reciprocal of the tap spacing is made proportional to distance along the line pair, the structure's local resonant frequency is a linear function of position, thus giving the linear group-delay-vs-frequency characteristic desired of the chimp filters within the analyzer. Amplitude weighting is achieved by appropriately varying the line separation s in the couplers. Details of modeling, design, and fabrication are given in Reference 14.

The devices used in the chimp-transform spectrum analyzer each contain 3.32 m of 39- μm -wide niobium stripline between 125- μm -thick silicon substrates, offering 37.5 ns of dispersion. The filters have a 2322-MHz bandwidth centered on 4000 MHz, giving a time-bandwidth (TB) product of 86.8. Flat-weighted and Hamming-weighted¹⁶ filters have been produced,¹⁷ each with 10-dB insertion loss. In pulse-compression tests using a flat-weighted device as an expander and a Hamming-weighted compressor, -24-dB sidelobe levels were demonstrated.¹⁷

The configuration used is shown in Figure 5-4. In this arrangement, termed the multiply-convolve arrangement⁹ because of the multiplication of the input signal by a chimp waveform followed by convolution of the product with the chimp impulse response of the compressor, the multiplying chimp is twice as long as the compression stage. Incoming CW signals ranging over a bandwidth equal to that of the compressor will therefore produce a chimp which fills the entire weighted aperture of the compressor.

Rather than provide a single expander with twice the dispersion and bandwidth (and thus four times the TB product) of the compressor, the impulse to be expanded is passed through two identical cascaded expanders with the same dispersion and bandwidth as the compressor and then through a frequency doubler. In fact, the impulse was passed through the same expander twice in succession.

The mixer used to multiply the premultiplying chimp and the RF input is a commercially available unit with broadband IF characteristics. All components, including amplifiers and filters not shown in Figure 5-4, operate at room temperature, except for the expander and compressor, which operate in liquid helium at 4.2 K.



137545-N-01

Figure 5-4. Chirp-transform spectrum analyzer employing superconductive expander and compressor. Frequency-time plots are shown for various points in the signal path. The RF signal input shown is an example of the possible signals within the $f_0 - B/2$ to $f_0 + B/2$ analyzer input band; in this case three tones are shown, one at f_0 , a second at $f_0 - B/2$, and a third at $f_0 + B/2$. These are mapped by the analyzer into time slots spaced by $T_c/2$.

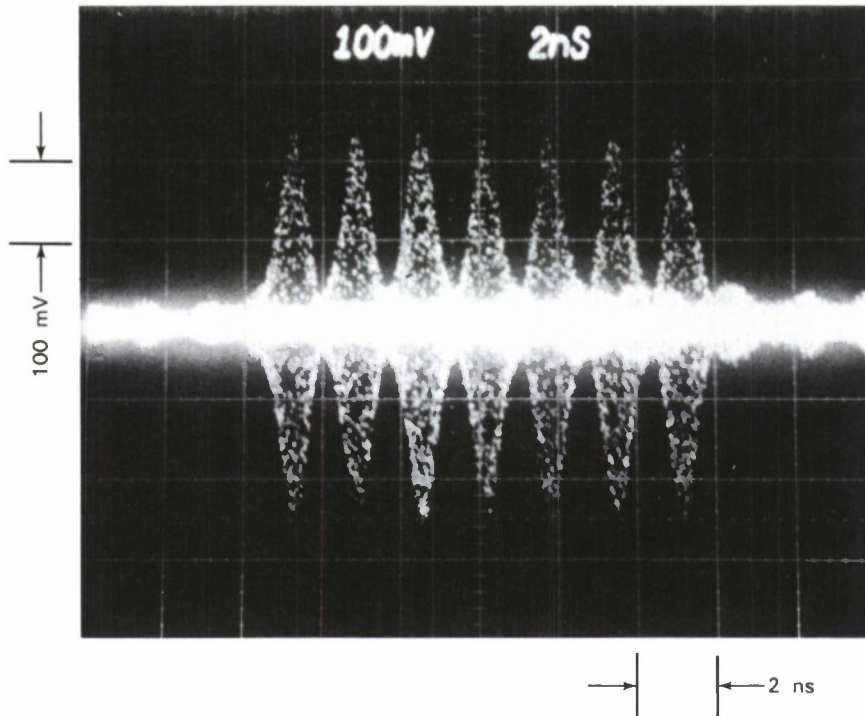


Figure 5-5. Multiple exposure of sampling-scope output for successive single-tone inputs of 4000 MHz (leftmost pulse) to 3400 MHz (rightmost pulse) in 100-MHz increments. The input power level is -7 dBm.

Figure 5-5 shows the compressor output in response to seven sequential CW tones from 3400 to 4000 MHz in 100-MHz increments. The system responds to RF inputs from 2.8 to 5.2 GHz with an amplitude uniformity of ± 1.2 dB. From the oscilloscope trace in Figure 5-5 the dispersion rate of the analyzer is measured to be 61 MHz/ns, in good agreement with the designed device chirp slope of 61.9 MHz/ns.

The width of the peaks at the -4-dB level is 0.7 ns, implying a two-tone frequency resolution of 43 MHz. For comparison, the expected resolution, which is the inverse of the compressor dispersion multiplied by a factor to account for the broadening caused by the Hamming weighting,¹⁶ is 39.2 MHz.

The compressor output amplitude is a linear function of the RF input amplitude for input power levels up to 3 dBm. Input CW signals of -43 dBm can be resolved from the noise floor set by the thermal noise of the room-temperature electronics, implying a dynamic range over the noise floor of 46 dB.

Sidelobe levels of 18 dB below the peak are observed. The dispersive delay lines themselves, in pulse compression tests, exhibit -24-dB sidelobes; thus, the added degradation is due to distortions in the room-temperature mixers, amplifiers, and filters.

Spectral analysis over a bandwidth of 2400 MHz with a resolution of 43 MHz and -18-dB sidelobe levels has been demonstrated using superconductive tapped electromagnetic delay lines. Reduction in sidelobe levels will result from improvements in substrate thickness uniformity, packaging tolerances, and room-temperature electronics. Design algorithms have been developed which permit the use of strongly tapped delay lines for low insertion losses (i.e., <3 dB) without the penalty of large phase distortions.¹⁸ Narrower frequency resolution will accompany the development of longer delay lines on thinner, larger, and/or stacked substrates. This technology is expected to eventually support bandwidths of 10 GHz and delay times of 500 ns or more.

Unlike the acoustooptic spectrum analyzer,¹² the output of the superconductive analyzer arrives in a serial stream at the full system bandwidth. To be practical for system applications, the output of such an analyzer will require high-speed sampling and thresholding circuitry. Although not yet available, superconductive digital electronics holds promise of providing such functions.

R. S. Withers
S. A. Reible

REFERENCES

1. D.J. Ehrlich and J.Y. Tsao, *J. Vac. Sci. Technol.* **B1**, 969 (1983).
2. R.C. Williamson, V.S. Dolat, and H.I. Smith, *1973 Ultrasonics Symposium Proceedings* (IEEE, New York, 1973), pp. 490-493.
3. D.J. Ehrlich and J.Y. Tsao, in *VLSI Electronics: Microstructure Science*, Vol. 7, N.G. Einspruch, Ed. (Academic, New York, 1983/1984).
4. D.J. Ehrlich, R.M. Osgood, Jr., and T.F. Deutsch, *Appl. Phys. Lett.* **38**, 1018 (1981).
5. D.J. Ehrlich and J.Y. Tsao, *Appl. Phys. Lett.* **44**, 267 (1984).
6. A.C. Anderson, V.S. Dolat, and W.T. Brogan, *1980 Ultrasonics Symposium Proceedings* (IEEE, New York, 1980), pp. 442-445.
7. T.A. Martin, *1976 Ultrasonics Symposium Proceedings* (IEEE, New York, 1976), pp. 411-414.
8. J.A. Edwards and M.J. Withers, *Proc. IEE* **114**, 1613 (1967).
9. G.W. Judd and V.H. Estrick, *Proc. SPIE* **239**, 220 (1980).
10. M.A. Jack, P.M. Grant, and J.H. Collins, *Proc. IEEE* **68**, 450 (1980).

11. D. Mergerian and E.C. Malarkey, *Acoustooptic Signal Processing*, N. Berg and J. Lee, Eds. (Dekker, New York, 1983).
12. L.C. Lennert, I.C. Chang, D.L. Steinmetz, W. Brooke, and F. Langdon, *Proc. SPIE* **352**, 10 (1982).
13. I.C. Chang and S. Lee, *1983 Ultrasonics Symposium Proceedings* (IEEE, New York, 1983), pp. 427-430.
14. R.S. Withers, A.C. Anderson, P.V. Wright, and S.A. Reible, *IEEE Trans. Magnetics* **MAG-19**, 480 (1983).
15. J.T. Lynch, R.S. Withers, A.C. Anderson, P.V. Wright, and S.A. Reible, *Appl. Phys. Lett.* **43**, 319 (1983).
16. C.E. Cook and M. Bernfeld, *Radar Signals* (Academic Press, New York, 1967).
17. R.S. Withers, A.C. Anderson, J.B. Green, and S.A. Reible, paper presented, 1984 Applied Superconductivity Conference, San Diego, California; to be published, *IEEE Trans. Magnetics* (1985).
18. R.S. Withers and P.V. Wright, *Proceedings of the 37th Annual Symposium on Frequency Control* (IEEE, New York, 1983), pp. 81-86.

UNCLASSIFIED

SECURITY CLASSIFICATION OF THIS PAGE (When Data Entered)

REPORT DOCUMENTATION PAGE		READ INSTRUCTIONS BEFORE COMPLETING FORM
1. REPORT NUMBER ESD-TR-84-327	2. GOVT ACCESSION NO.	3. RECIPIENT'S CATALOG NUMBER
4. TITLE (and Subtitle) Solid State Research		5. TYPE OF REPORT & PERIOD COVERED Quarterly Technical Report 1 November 1984 — 31 January 1985
		6. PERFORMING ORG. REPORT NUMBER 1985:1
7. AUTHOR(s) Alan L. McWhorter		8. CONTRACT OR GRANT NUMBER(s) F19628-85-C-0002
9. PERFORMING ORGANIZATION NAME AND ADDRESS Lincoln Laboratory, M.I.T. P.O. Box 73 Lexington, MA 02173-0073		10. PROGRAM ELEMENT, PROJECT, TASK AREA & WORK UNIT NUMBERS Program Element No.63250F Project No.649L
11. CONTROLLING OFFICE NAME AND ADDRESS Air Force Systems Command, USAF Andrews AFB Washington, DC 20331		12. REPORT DATE 15 February 1985
		13. NUMBER OF PAGES 84
14. MONITORING AGENCY NAME & ADDRESS (if different from Controlling Office) Electronic Systems Division Hanscom AFB, MA 01731		15. SECURITY CLASS. (of this Report) Unclassified
		15a. DECLASSIFICATION DOWNGRADING SCHEDULE
16. DISTRIBUTION STATEMENT (of this Report) Approved for public release; distribution unlimited.		
17. DISTRIBUTION STATEMENT (of the abstract entered in Block 20, if different from Report)		
18. SUPPLEMENTARY NOTES None		
19. KEY WORDS (Continue on reverse side if necessary and identify by block number)		
solid state devices	photodiode devices	infrared imaging
quantum electronics	lasers	surface-wave transducers
materials research	laser spectroscopy	charge-coupled devices
microelectronics	imaging arrays	acoustoelectric devices
analog device technology	signal processing	
20. ABSTRACT (Continue on reverse side if necessary and identify by block number)		
<p>This report covers in detail the solid state research work of the Solid State Division at Lincoln Laboratory for the period 1 November 1984 through 31 January 1985. The topics covered are Solid State Device Research, Quantum Electronics, Materials Research, Microelectronics, and Analog Device Technology. Funding is primarily provided by the Air Force, with additional support provided by the Army, DARPA, Navy, NASA, and DOE.</p>		